# THz-TDS Characterization of the Digital Communication Channels of the Atmosphere and the Enabled Applications

**Yihong Yang, Mahboubeh Mandehgar & D. Grischkowsky**

**Journal of Infrared, Millimeter, and Terahertz Waves**

ISSN 1866-6892

J Infrared Milli Terahz Waves
DOI 10.1007/s10762-014-0099-3

Springer

J Infrared Milli Terahz Waves
DOI 10.1007/s10762-014-0099-3

# THz-TDS Characterization of the Digital Communication Channels of the Atmosphere and the Enabled Applications

**Yihong Yang · Mahboubeh Mandehgar ·
D. Grischkowsky**

Received: 7 April 2014 / Accepted: 29 July 2014

**Abstract** Our measurements and complete linear dispersion theory calculations of amplitude and phase show that it is possible to have seven high performance point-to-point, 10.7 Gb/s to 28.4 Gb/s, digital THz ground links in the atmosphere. At a RH 58% (10g/m$^3$) and 20 °C including $O_2$ absorption, and for an absorption loss of 10 dB, the seven links are: Channel 1: at 96 GHz, Bandwidth (BW) 30 GHz, 10.7 Gb/s for 17.5 km, Channel 2: at 144 GHz, BW 30 GHz, 12.0 Gb/s for 7.4 km, Channel 3: at 252 GHz, BW 50 GHz, 25.2 Gb/s for 2.5 km, Channel 4: at 342 GHz, BW 24 GHz, 11.4 Gb/s for 840 m, Channel 5: at 408 GHz, BW 30 GHz, 13.6 Gb/s for 440 m, Channel 6: at 672 GHz, BW 60 GHz, 22.6 Gb/s for 140 m, and Channel 7: at 852 GHz, BW 60 GHz, 28.4 Gb/s for 120 m.

The enabled long-path THz links are discussed. Two applications are presented in detail, namely, a long-path 17.5 km THz ground-link operating at 96 GHz, BW 30 GHz, 10.7 Gb/s, and a GEO satellite link at 252 GHz, BW 50 GHz, 25.2 Gb/s. In addition, Channel 7 at 852 GHz is studied by calculated pulse propagation to understand the relationships between high bit-rates and propagation distance. It is shown that good digital transmission could be obtained with 852 GHz, BW 108 GHz, 56.8 Gb/s for a 160 m propagation distance in the atmosphere with RH 58% (10g/m$^3$) and 20 °C. Good digital transmission could also be obtained with 852 GHz, BW 108 GHz, 71.0 Gb/s for 80 m. These results are discussed with respect to high bit-rate, short-path applications.

These digital THz communication channels were determined together with a new measurement of the water vapor continuum absorption from 0.35 to 1 THz. The THz pulses propagate though a 137 m long humidity-controlled chamber and are measured by THz time-domain spectroscopy (THz-TDS). The average relative humidity along the entire THz path is precisely obtained by measuring the difference between transit times of the sample and reference THz pulses to an accuracy of 0.1 ps. Using the measured total absorption and the calculated resonance line absorption with the Molecular Response Theory lineshape, an accurate continuum absorption is obtained within five THz absorption windows, that agrees with the empirical theory.

---

Y. Yang · M. Mandehgar · D. Grischkowsky (✉)
School of Electrical and Computer Engineering, Oklahoma State University, Stillwater, OK 74078, USA
e-mail: daniel.grischkowsky@okstate.edu

**Keywords** THz Wireless Communications · Continuum Absorption of Water Vapor · THz Windows in the Atmosphere · THz transmission through rain · THz Scintillations in Atmosphere · THz Wireless Simulations

## 1 Introduction

An important problem for the operating world-wide telecommunications network is to provide isolated cities, islands, communities, remote industrial, technical and scientific sites with wideband access to the fiber backbone [1–8]. Currently, their best access is with microwave ground links or satellite links. Another long-standing problem is to be able to provide emergency, high-bandwidth back-up service for the loss of an optical fiber link. Another problem is to provide older large office buildings in cities, sport stadiums and shopping malls with full high bandwidth services. Here, we describe the potential of wireless THz ground links or satellite links to provide low loss, high bandwidth digital connections, as possible solutions to these and other problems [1–8].

Water vapor controls the propagation of THz waves in the atmosphere. All considered technical, commercial and research applications of THz waves depend on the variable amount of water vapor. The humidity changes strongly with the daily weather, changing seasons, altitude and geographical location. The propagation of THz waves in the atmosphere is limited by the water vapor absorption, from hundreds of strong rotational lines surrounded by thousands of weaker lines from the mm wave range through the terahertz region up to 5 THz. Also, oxygen gas has a cluster of approximately 25 overlapping lines at 60 GHz, a weak single line at 120 GHz, and a weak three line repetitive structure every 350 GHz extending to well beyond 2 THz. Many strong absorption lines are separated by windows of transparency dividing the spectrum into sections from mm waves into the THz range and up to 5 THz. However, an additional continuum absorption exists over this range and within the mm and THz windows, which cannot be explained by the far-wing absorption of the resonant lines. In addition, the group velocity dispersion reshapes the propagated pulses. Measurements and understanding of the continuum absorption are important in many aspects of physics and applications of the atmosphere, such as ground and satellite-based radio astronomy [17], communication links [3], and remote spectroscopic applications [18].

Figure 1 shows the enormous variation of THz power attenuation (dB/km) over the frequency range from 50 GHz to 1000 GHz. The attenuation changes by 5 orders of magnitude from maximum to minimum over this frequency range. Curve A in Fig. 1. is the sum of the calculated attenuation of all the water rotational lines, plus the much weaker continuum attenuation shown as curve B, which is considered to be due to water dimers, higher-order clusters, and self-broadening of the strong water lines [9]. The attenuation due to the water lines increases linearly with the number density of water vapor, while one part of the continuum attenuation increases as the square of the number density. Consequently, the relative proportion of the total absorption due to the continuum increases with the number density. Many simulation codes have been developed to model the absorption of THz radiation by water vapor in the atmosphere [19, 20], and an important example is shown in Fig. 2 [20].

The shaded lines numbered 1-7 in Figs. 1 and 2, indicate the digital communication channels, which are the subject of this paper. We will present new experimental measurements of these windows of transparency in the atmosphere and the associated continuum absorption. We will also simulate the propagation of a bit pulse sequence through all of these seven

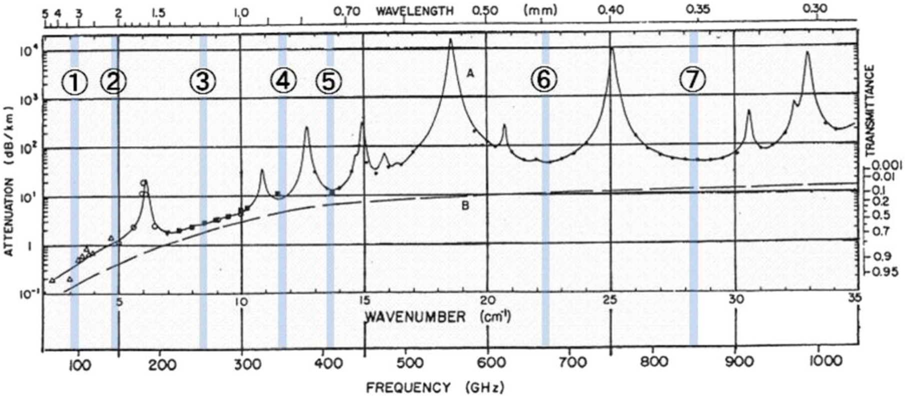

**Fig. 1** This figure is a revised version of Fig. 10 of [9]. "Spectral plots of the near-millimeter attenuation by the atmospheric $H_2O$ at sea level. $H_2O$ density = 5.9 g/m$^3$. Curve A represents attenuation calculated by summing the theoretical contributions by all the lines and adding the continuum represented by curve B." [9]. The $H_2O$ density corresponds to a relative humidity of 34% at 20 °C. The indicated measurements have been made by several groups; the open triangles below 150 GHz are from Dryagin et al. [10]; the open circles below 200 GHz are from Frenkel and Woods [11]; the filled triangle at 200 GHz is from Straiton and Tolbert [12]; the filled squares from 200 to 400 GHz are from Ryadov and Furashov [13], and the solid circles from below 400 GHz to 1000 GHz are from Burch [14, 15]. 7 water windows (circled numbers) are marked for comparison with the THz-TDS measurements. (Adapted from [16])

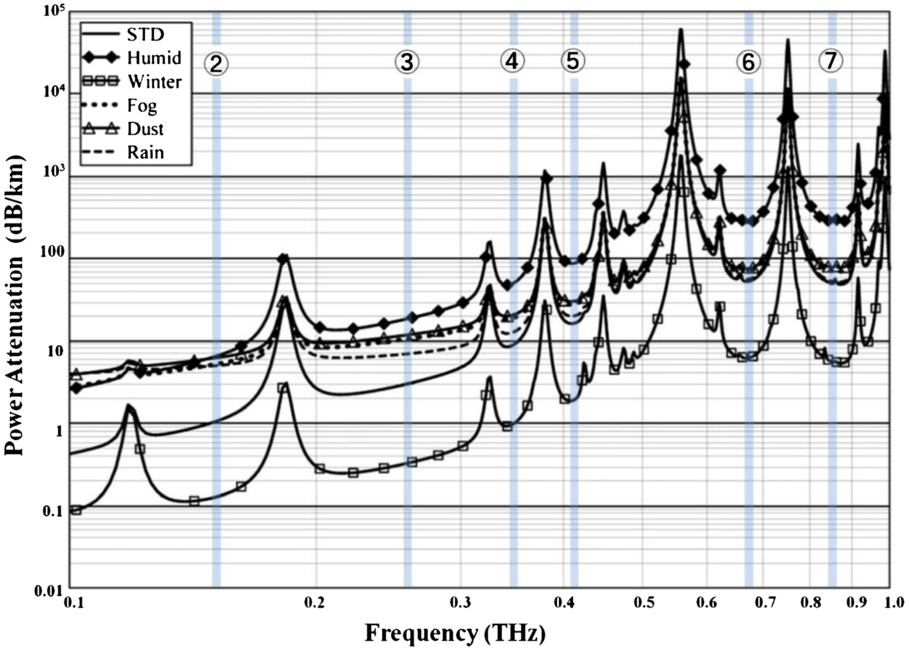

**Fig. 2** Atmospheric attenuation at sea level for different conditions of temperature, relative humidity (RH), fog, dust and rain. (STD: 20 °C, RH 44%), (Humid: 35 °C, RH 90%), (Winter: -10 °C, RH 30%), (Fog, Dust, and Rain: 20 °C, RH 44%) (Rain at 4 mm/hr.), (Fog at 100 m visibility), (Dust at 10 m visibility). Revised figure taken from Ref. 16. Six water windows (circled numbers) are marked for comparison with the THz-TDS measurements. (Adapted from [20])

windows with the different lengths in the atmosphere at RH 58% at 20 °C (density of 10 g/m$^3$) giving 10 dB attenuation for the particular channel. The simulated bit-rates range from 10.7 Gb/s to 28.4 Gb/s, depending on the group velocity dispersion of the particular channel, and the bandwidth of the window.

The empirically determined continuum absorption is usually defined as the difference between the measured total absorption and the absorption of the resonant lines [21]. The resonant lines absorption can be calculated as the sum of all of the individual resonant lines. For each line, the corresponding line intensity and linewidth can be found in a spectroscopic database, such as the Millimeter wave Propagation Model (MPM) [22], HITRAN [23] and JPL [24], and used with the lineshape function to obtain the resonant line absorption. Consequently, the determined continuum absorption depends strongly on the lineshape function and spectroscopic database, which provides the number of lines, line intensities and linewidth for the line-by-line summation method.

As shown in Fig. 3 [25], our first long-path measurement was the passage of transform limited 1 ps THz pulses through a 167 m round-trip optical path, where the pulse absorption and reshaping was caused by the atmospheric water vapor with RH 51% at 21°C. The stable pulseshape feature at the front of the transmitted pulse in Fig. 3a, appeared to have propagated through the water vapor with very little loss and dispersion [25]. This stable pulseshape propagation was shown to have the highlighted coherent spectrum denoted as I and II in Fig. 3b, describing two over-lapping transform limited pulses (THz bit pulses I and II), respectively. Using each of these pulses as the input pulse to linear dispersion theory calculations of additional long propagation lengths, showed they had remarkable stability and relatively low loss [21, 25].

In this paper, we report new measurements of the relative total water vapor absorption, using a 137 m round-trip humidity controlled sample chamber within the 170.4 m long-path THz-TDS system, that measures the water density from the transit time of the THz pulses [26]. For our analysis, we use the fundamental molecular response theory (MRT) [27–29], based on physical principles and measurements, to obtain the resonant line absorption.

## 2 Theory

The determined continuum absorption depends strongly on the lineshape function, number of lines, line intensities and linewidth chosen for the line-by-line summation method. It has been shown that the van Vleck-Weisskopf (vV-W) lineshape fits the resonant lines near their centers more accurately than the full Lorentz (FL) and Gross lineshapes [30]. Since then, in most of the literature the vV-W lineshape has been used to obtain the continuum absorption within the Millimeter wave [22, 31, 32] and THz regions [33–35] under various humidity and temperature conditions.

Recently it has been shown that the Molecular Response Theory (MRT) lineshape is the best model to fit the absorption line [29]. Through a weighting factor, the MRT lineshape function smoothly changes from the van Vleck-Weisskopf (vV-W) lineshape [36] near the line center to the full Lorentz (FL) lineshape [36] at far wings of the resonance line. The MRT lineshape overcomes the disadvantage of the unphysical far-wing of the vV-W lineshape, as well as the underestimated absorption from the vV-W lineshape with a cutoff. Clearly, resonance absorption with a strictly defined lineshape function is needed for reliable and comparable values of the continuum absorption.

The spectroscopic databases of MPM, JPL and HITRAN provide 30, 3085, and 8678 water vapor absorption lines up to 1, 30, and 30 THz, and 44, 259, and 4679 oxygen

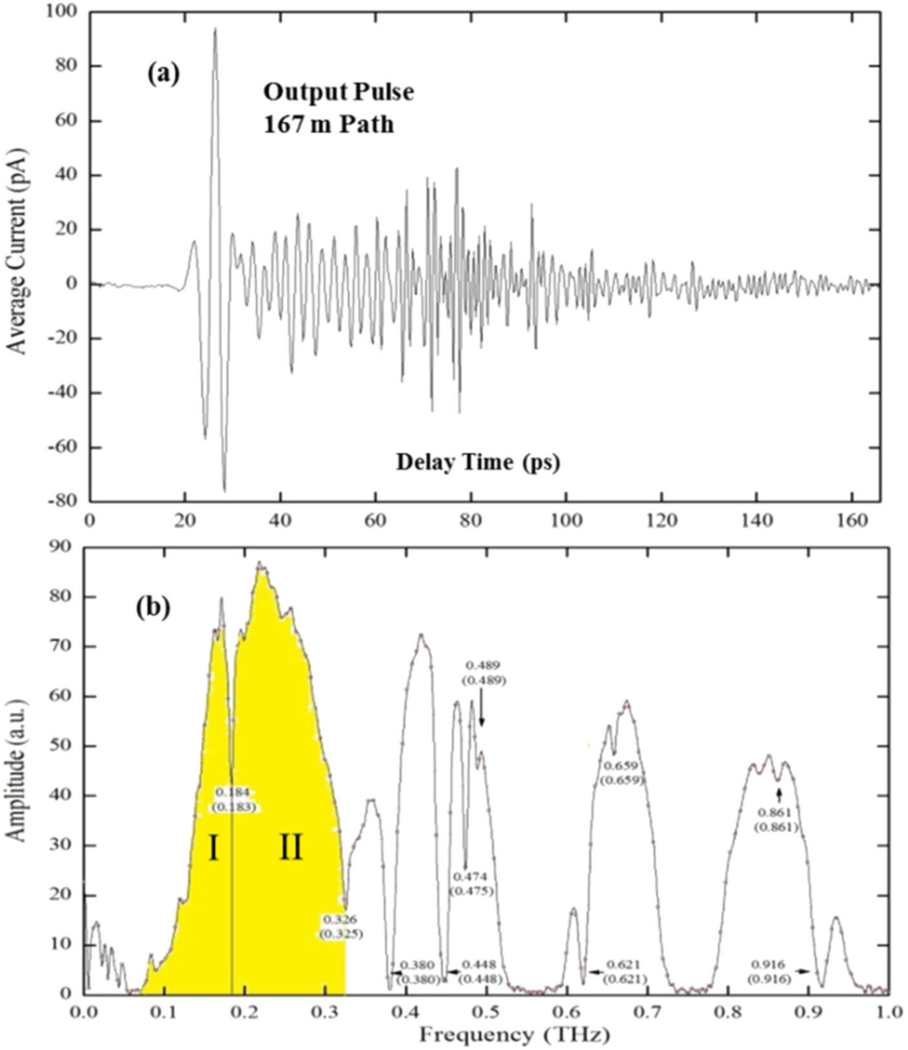

**Fig. 3** (a) Transmitted THz pulse. Inset shows the input THz pulse together with the much smaller THz output pulse. (b) Amplitude spectrum of Transmitted pulse. Regions I and II mark the atmospheric communication channels I and II. Inset shows the input spectrum and the much smaller output spectrum. (Adapted from [25])

absorption lines up to 1, 11, and 8 THz, respectively. The necessity to include strong absorption lines above 1 THz of our upper limit, is due to the strong effects on the attenuation and phase from their far wing absorption, which is shown in our previous work on water vapor refractivity [26, 37]. Moreover, the linewidths of resonant absorption lines are also sensitive to the relative pressure and the ambient air pressure. HITRAN is the only database to provide the factors of air-broadened width and self-broadened width, which can be used to calculated the linewidths of all the absorption lines. Consequently, the HITRAN database is chosen for our simulations to provide the most accurate model for THz wireless applications.

### 2.1 Molecular Response Theory

For the molecular response theory the absorption coefficient of a resonant line is given by [27–29]

$$\alpha_j^{MRT}(\nu) = S(\nu)\alpha_j^{vV-W}(\nu) + (1-S(\nu))\alpha_j^{L}(\nu). \tag{1}$$

for which $\alpha_j^{vV-W}(v)$ is the absorption coefficient with the vV-W lineshape function and $\alpha_j^{L}(v)$ is the absorption coefficient with the FL lineshape function. $S(v)$ is the MRT weighting function controlling the transition from the vV-W lineshape at low frequencies to the FL lineshape at higher frequencies. $S(v)$ is given simply by,

$$S(\nu) = 1/\left[1 + (2\pi\nu\tau_c)^2\right]. \tag{2}$$

where $\tau_c$ is the collision parameter, considered to be a measure of the orientation time of molecules during a collision and expected to be much faster than the duration of a collision. The weighting function $S(v)$ monotonically changes from one to zero as the frequency increases, and $S(\nu) = 0.5$ for $\nu_{1/2} = 1/(2\pi\tau_c) = 796$ GHz for $\tau_c = 0.2$ ps [27, 28]. Consequently, for $2\pi\nu\tau_c \ll 1$, $\alpha_j^{MRT}(\nu) \approx \alpha_j^{vV-W}(\nu)$, and for $2\pi\nu\tau_c \gg 1$, $\alpha_j^{MRT}(\nu) \approx \alpha_j^{L}(\nu)$. It is important to note that the MRT line, as defined in Eq. (1), will always be between the FL and the vV-W lines [27–29]. Only the half-width at half-maximum $\Delta v_j$ linewidths of the vV-W and FL lineshapes remain as parameters, and these are calculated by HITRAN as $\Delta v_j = \gamma_{ks}P_s + \gamma_{kf}P_f$ with $\gamma_{ks}$ and $\gamma_{kf}$ are the self and foreign gas line broadening coefficients [29, 35].

### 2.2 Empirical Continuum absorption function

The empirical equation of the continuum absorption $\alpha_c$ has been experimentally verified [22, 31, 38] to have a quadratic frequency dependence and to be a combination of two ambient air pressure terms, as shown in Eq. (3). One term is proportional to the square of the water vapor partial pressure $P_W$; the other term is proportional to the product of $P_W$ and the total of the foreign gas partial pressures in the atmosphere $P_A$.

$$\alpha_c(v, 294K) = v^2\left[C_W^*\cdot\rho_W^2 + C_A^*\cdot\rho_A\cdot\rho_W\right]. \tag{3}$$

where $C_W^*$ and $C_A^*$ are the self and foreign continuum parameters at 294 K in units of dB/km/(GHz g/m$^3$)$^2$. The multiplication factor of 0.752 converts the water vapor pressure $P_W$ in hPa to density $\rho_W$ in g/m$^3$. Similarly, the multiplication factor for air is 1.19. The normal atmospheric pressure $P_A$ = 1004 hPa, equivalent to the density $\rho_A$ =1193 g/m$^3$, can be considered constant, since the variable water vapor partial pressure $P_W$ is only of the order of 1% of $P_A$. All of parameters used in Eq. (3) are discussed in detail in Ref. 29. This empirical equation shows good agreement with experiments results at high water vapor pressure and high temperature measurements over a wide range [22, 31, 38].

Similar to our previous work [29], we measured the total absorption $\alpha^S$ and $\alpha^R$ of the humid air sample signal and the dry air reference signal, and obtained the relative absorption $\Delta\alpha_x$ between the sample and reference signals with different humidity levels. Since the absorption is the sum of the MRT resonant line absorption and the continuum absorption, the relative absorption consists of the MRT resonant line absorption $\alpha_{MRT}^S - \alpha_{MRT}^R$ and the continuum absorption $\alpha_c^S - \alpha_c^R$. The relative resonance line absorption $\Delta\alpha_{MRT} = \alpha_{MRT}^S - \alpha_{MRT}^R$ is linearly proportional to water vapor density. However, due to the quadratic part of water vapor partial pressure in the continuum absorption empirical equation, a cross term was brought into the measured relative continuum absorption $\Delta\alpha_{cx}$. Based on Eq. (3), the relative continuum absorption $\Delta\alpha_{cx}$ including the cross term is given by,

$$\Delta\alpha_{cx} = \alpha_c^S - \alpha_c^R = \nu^2\left[C_W^*\cdot\left(\left(\rho_W^S\right)^2 - \left(\rho_W^R\right)^2\right) + C_A^*\cdot\rho_A\cdot\left(\rho_W^S - \rho_W^R\right)\right]. \tag{4}$$

where $\rho_W^S$ and $\rho_W^R$ denotes water vapor density of the humid sample and dry reference signals respectively, and the cross term function $X$ is given by

$$X = \nu^2 C_W^*\left(2\rho_W^R\Delta\rho_W\right). \tag{5}$$

The cross term $X$ has to be subtracted from the relative continuum absorption $\Delta\alpha_{cx}$ and from the relative total absorption $\Delta\alpha_x$. Eqs. (6a) and (6b) give the continuum absorption $\Delta\alpha_c$ and the total absorption $\Delta\alpha$, which only depends on $\Delta\rho_W$.

$$\Delta\alpha_c = \Delta\alpha_{cx} - X = \nu^2\left[C_W^*\cdot\Delta\rho_W^2 + C_A^*\cdot\rho_A\cdot\Delta\rho_W\right]. \tag{6a}$$

$$\Delta\alpha = \Delta\alpha_x - X. \tag{6b}$$

The value of the water vapor density of the reference THz signal $\rho_W^R$ in the additional cross term $\rho_W^R\Delta\rho_W$ can be obtained from the water vapor partial pressure measured by hygrometers in the sample chamber.

In the previous work [29], the lowest dry reference signal had a RH of 22.2% at 21°C (corresponding to a water vapor density of 4.1 g/m$^3$), which gave a cross-term with power attenuation of 23% of the total continuum absorption before subtracting the cross-term for 7.0 g/m$^3$ water vapor density (corresponding to a RH difference of 38.2%).

In order to obtain higher accuracy values of the water vapor continuum absorption, it is important to have low RH dry reference signals in the experiments. For the two measurements described here, RH of 13% and RH 8% at 21°C were obtained, corresponding to the reference water vapor densities $\rho_W^R$ of 2.3 g/m$^3$, and = 1.4 g/m$^3$. Consequently, the corresponding cross terms X are much reduced from the earlier measurement [29].

## 3 Experimental Methods

Figure 4 shows the long-path THz system for the experimental measurements of continuum absorption described in [25, 26]. The 170.4 m round-trip, long-path THz setup is coupled to the standard THz time domain spectroscopy (THz-TDS) system [39]. It is noteworthy that the long-path THz setup distance of 170.4 m is designed to be within 15 cm to an integer multiple (51 in this case) of the mode-locked laser pulse round-trip path of 3.342 m with a repetition rate of 89.6948 MHz for coherent detection with a high signal-to-noise ratio. The THz signals propagate 137 m within the controlled RH sample chamber (shown by the red box), which is transformed from the lab hallway by sealing doors and vents during measurements. A recent improvement of the sample chamber covered the ceiling with thin plastic sheets, supported by hundreds of button magnets. This enabled repeatable and stable 60% RH increases from the reference RH, as well as a doubling of the water vapor holding time of the chamber. The chamber RH was controlled by 10 humidifiers and 5 fans distributed uniformly to obtain good air circulation; the constant temperature was maintained by building facilities.

The transit time of THz pulses propagated through THz long-path system is measured to a precision of 0.1 ps by the THz-TDS system, using the mode-locked laser as an optical clock.

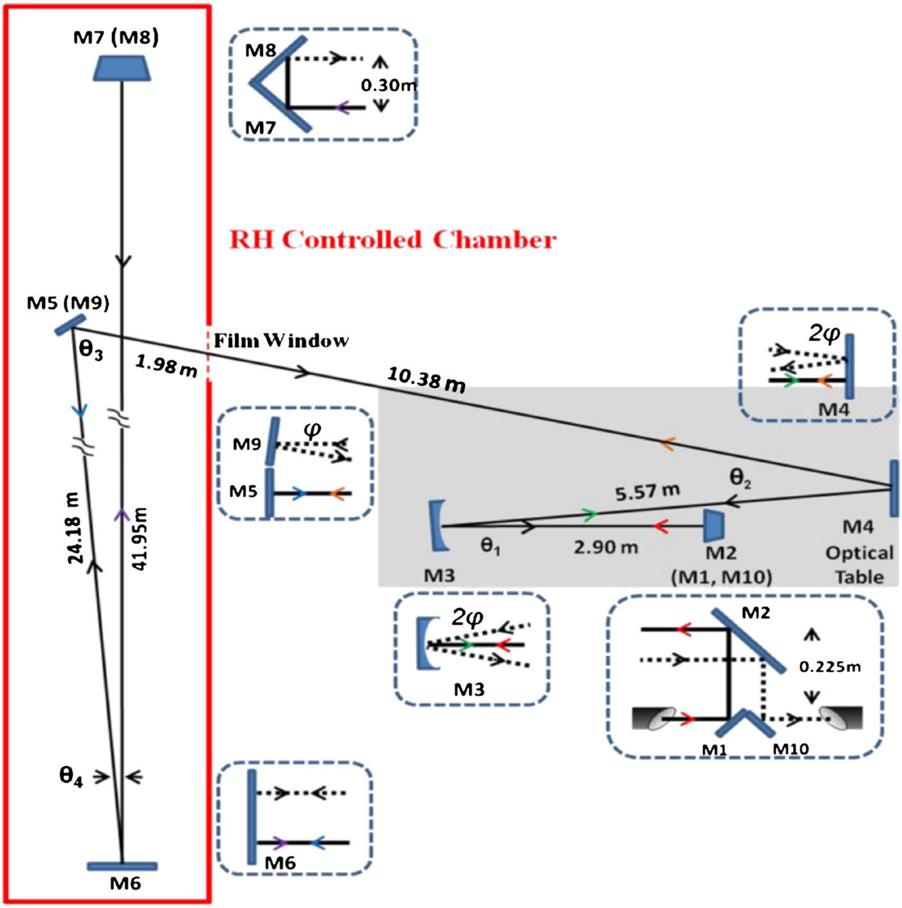

Fig. 4 Experimental setup with 170 m long-path system

The transit time has been shown to have a linear relation with the RH (water vapor density) inside the sample chamber [26]. However, slow drifts of the long THz optical train and mode-locked laser can affect the precision of the measured transit times. The slow length drift of long THz optical train is mainly due to the heat expansion and cold contraction of the concrete floor and stainless steel (SS) optical table, corresponding to a 5.7 ps change, for a 1 °C change of their temperature difference. This agrees with the observed day to day and week to week changes [25, 26]. The mode-locked laser has a frequency drift in the optical clock rate of the order of 100 Hz. However, the measured weak water vapor absorption line center frequencies agree with the HITRAN and the JPL databases to an accuracy of 1 GHz [25], indicating negligible mode-locked laser drift within several scans.

The input THz pulses shown in Fig. 5 were measured with the kinematic M3-M10 mirror assembly removed. Then the kinematic M3-M10 assembly was replaced, and the THz pulses transmitted through the 170.4 m long-path were measured.

The measured THz pulses and their corresponding Fourier-transformed frequency spectra are shown in Figs. 6 and 7, for two groups of measurements taken on two different days, 7 days apart. The measured THz pulses in each group were recorded from the same start position of the time scan, which allowed the determination of the transit time difference between the

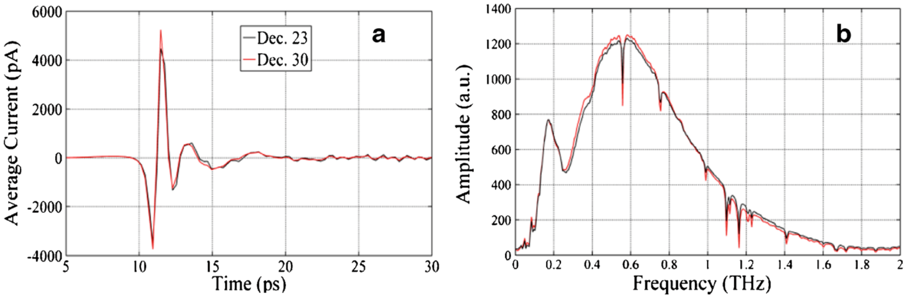

**Fig. 5** (a) Input THz pulses to mirror M1 for the two different measurements. (b). Corresponding amplitude spectra

THz pulses with specified RH, as shown in Figs. 6a and 7a. The time values in ps at the beginning of the THz signals are the transit times from the starting position. The frequency spectra in Figs. 6b and 7b are averages of three THz pulses in each set.

The frequency independent part of water vapor refractivity is (n-1) = 61.6 × $10^{-6}$ in an atmosphere with RH 58% at 20 °C (density of 10 g/$m^3$) [37]. The transit time of THz pulses through the 137 m total round-trip path with RH 58% at 20 °C (density of 10 g/$m^3$) in the chamber is 27.9 ps longer, than for a dry chamber. By comparing the transmitted time difference $\Delta t$ of the sample and reference pulses with 27.9 ps / 10 g/$m^3$, the relative water vapor density can be calculated to an accuracy of 0.04 g/$m^3$, corresponding to RH 0.2%, and a 0.1 ps delay change.

From the experimental results, for a long-time period (several tens of minuets), the stable transit times for several continuous scans in a series show the stability of the optical train of the long-path setup. For a short-time period (<3 min), the center frequencies of measured weak water vapor absorption line in the Fourier-transformed frequency spectra shown in Figs. 6 and 7, agree with the HITRAN and the JPL database to an accuracy of 1 GHz [25], which indicates no significant laser-clock drift.

## 4 Results

The relative amplitude transmission of sample with respect to the reference of for the path length of 137 m was obtained by dividing the sample amplitude spectra by the reference spectra that are shown in Figs. 6b and 7b. The corresponding power absorption $\Delta\alpha_x$ shown as black solid line and circles in Figs. 6c and 7c were obtained by taking the log to the base 10 of the values of transmission per km, multiplied by 20.

Using HITRAN database and MRT theory with same water vapor density as experiments, the relative resonance line absorption $\Delta\alpha_{MRT}=\alpha^S_{MRT}-\alpha^R_{MRT}$ were calculated and plotted as the red solid curves shown in Figs. 6c and 7c.

It is noteworthy that oxygen absorption lines are not considered in MRT simulation since the only variable in experiments is the amount of water vapor. But for the demonstration of atmospheric THz wireless communication channels shown in Fig. 9, all of the water vapor resonant absorption, continuum absorption and oxygen resonant absorption are considered.

According to the accepted definition, the continuum absorption with cross-term can be obtained by simply calculating the difference between $\Delta\alpha_x$ and $\Delta\alpha_{MRT}$ at all available THz windows. Then, subtracting the cross-tem which defined by Eq. (5), the continuum absorption was determined and shown in Fig. 8, in a good agreement compared to the empirical equation fitting curve.

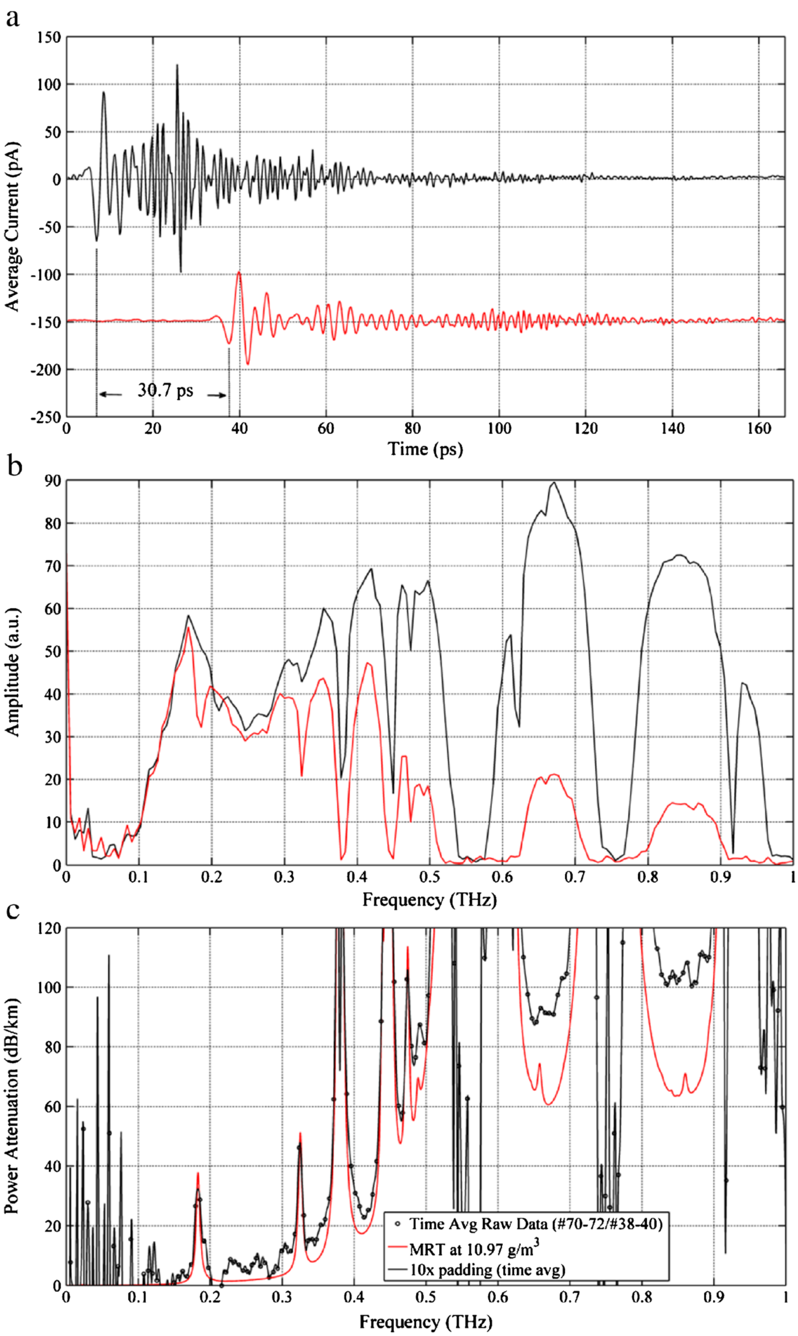

**Fig. 6** (a) Measured THz pulses transmitted through the 137 m sample chamber at RH 13% at 21 °C (black upper reference pulse) and at RH 71% at 21 °C (red lower sample pulse). The difference in transit times between the reference and samples pulse is 30.7 ps corresponding to a change in water vapor density of $\Delta\rho = 11.0\ \mathrm{g/m^3}$. (b) Corresponding amplitude spectra (with no zero padding) for the reference pulse (black upper spectrum) and the sample pulse (red lower spectrum). (c) Corresponding measured absorption in dB/km (open circles) compared to MRT theory, for which the difference is the continuum absorption plus the cross-term X

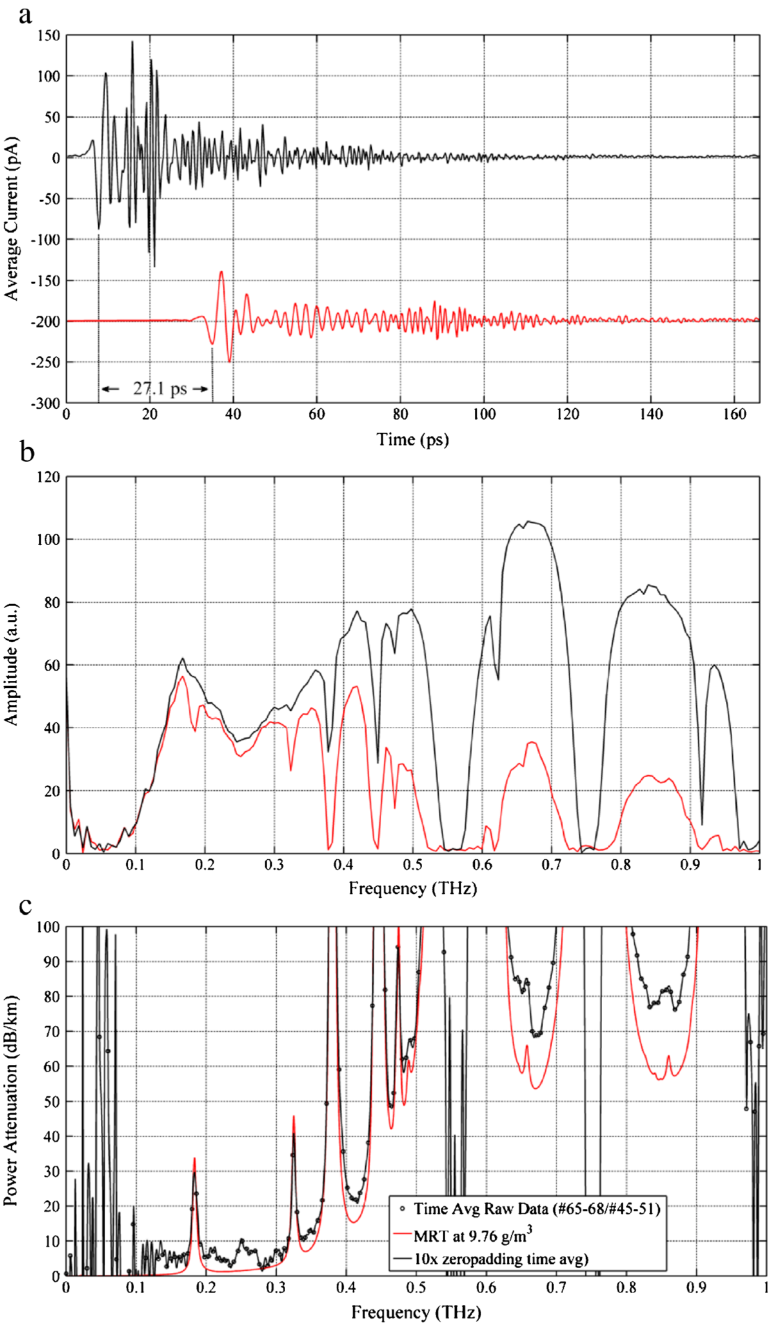

**Fig. 7** (a) Measured THz pulses transmitted through the 137 m sample chamber at RH 8% at 21 °C (black upper reference pulse) and at 65% at 21 °C (red lower sample pulse). The difference in transit times between the reference and samples pulse is 27.1 ps corresponding to a change in water vapor density of $\Delta\rho = 9.8$ g/m$^3$. (b) Corresponding amplitude spectra (with no zero padding) for the reference pulse (black upper spectrum) and the sample pulse (red lower spectrum). (c) Corresponding measured absorption in dB/km (open circles) compared to MRT theory, for which the difference is the continuum absorption plus the cross-term X

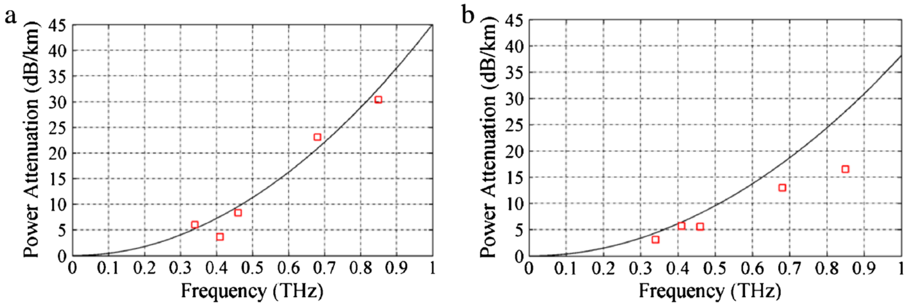

**Fig. 8** (a) The determined water vapor continuum absorption at five THz windows (red open squares) compared to the empirical equation for measurements ($\Delta\rho = 11.0$ g/m$^3$) shown in Fig. 6. (b) The determined water vapor continuum absorption at five THz windows (red open squares) compared to the empirical equation for measurements ($\Delta\rho = 9.8$ g/m$^3$) shown in Fig. 7

In Fig. 8 the values of the continuum absorption from the measurements of Figs. 6 and 7 are compared with the empirical theory of Eq. (3), using the same values of the parameters $C^*_W$ and $C^*_A$ , that were determined in Ref. 29. These same parameters were also used to calculate the continuum absorption shown in Fig. 9a.

As shown on Fig. 9a, the center frequencies of the seven digital communication channels are located in the windows of transparency. In addition, for broad-band digital communications, the center frequencies are also located at the minimum values of GVD within the windows to minimize pulse broadening. These seven center frequencies are also indicated on the GVD curve of Fig. 9c, and will be discussed in more detail below.

For the absorption shown in Fig. 9a, it is informative to compare the ratio of the MRT resonant line absorption to the empirically fit continuum absorption, $R_\alpha = \alpha_{MRT} / \alpha_c$, for the THz windows of transparency: at 852 GHz, $R_a = 2.03$, at 672 GHz, $R_a = 3.10$, at 408 GHz, $R_\alpha = 2.37$, at 342 GHz, $R_\alpha = 1.57$, at 252 GHz, $R_\alpha = 0.62$, at 145 GHz, $R_\alpha = 0.59$, and at 95 GHz, $R_\alpha = 0.42$. For the windows below 300 GHz, as the frequency is reduced the continuum absorption becomes larger than the MRT absorption. This situation has driven much interest in mm wave applications, for which the continuum absorption is the major component.

The discussion of the communication channels will now be given in two adjoining frequency domains. The first domain covers the frequency range from 0 to 400 GHz, and the second domain covers the range from 400 to 1000 GHz.

In Fig. 10a, we show the MRT-HITRAN calculation (red line) and the earlier vV-W-JPL calculation (black line) [40] of water vapor and oxygen plus the continuum amplitude transmission through 2 km of the atmosphere. The continuum amplitude transmission components obtained from Eq. (6a) are 0.921 at 95 GHz, 0.826 at 145 GHz, 0.567 at 250 GHz, and 0.339 at 345 GHz. In Fig. 10 (a) these transmission values were multiplied by the corresponding MRT-HITRAN values for the H2O plus O2 vapor transmission of 0.952 at 95 GHz, 0.885 at 145 GHz, 0.697 at 250 GHz, and 0.182 at 345 GHz to obtain 0.877, 0.731, 0.395, and 0.062, respectively. The attenuation of the proposed links are more limited by the water continuum absorption, than by the water vapor and oxygen vapor absorption.

Figure 10b shows the corresponding vV-W-HITRAN (red line) and the vV-W-JPL (black line) phase calculations for a path length of 2 km at RH 57.8% and 20°C (10 g/m$^3$) and oxygen. For channels 1-3, the phase is also shown for a 10 km propagation. The new vV-W-HITRAN phase calculation gives excellent agreement with the earlier vV-W-JPL calculation [40].

We obtain the group velocity dispersion (GVD) for the seven channels by taking the numerical second derivative with respect to angular frequency of the phase curve in Fig. 9b.

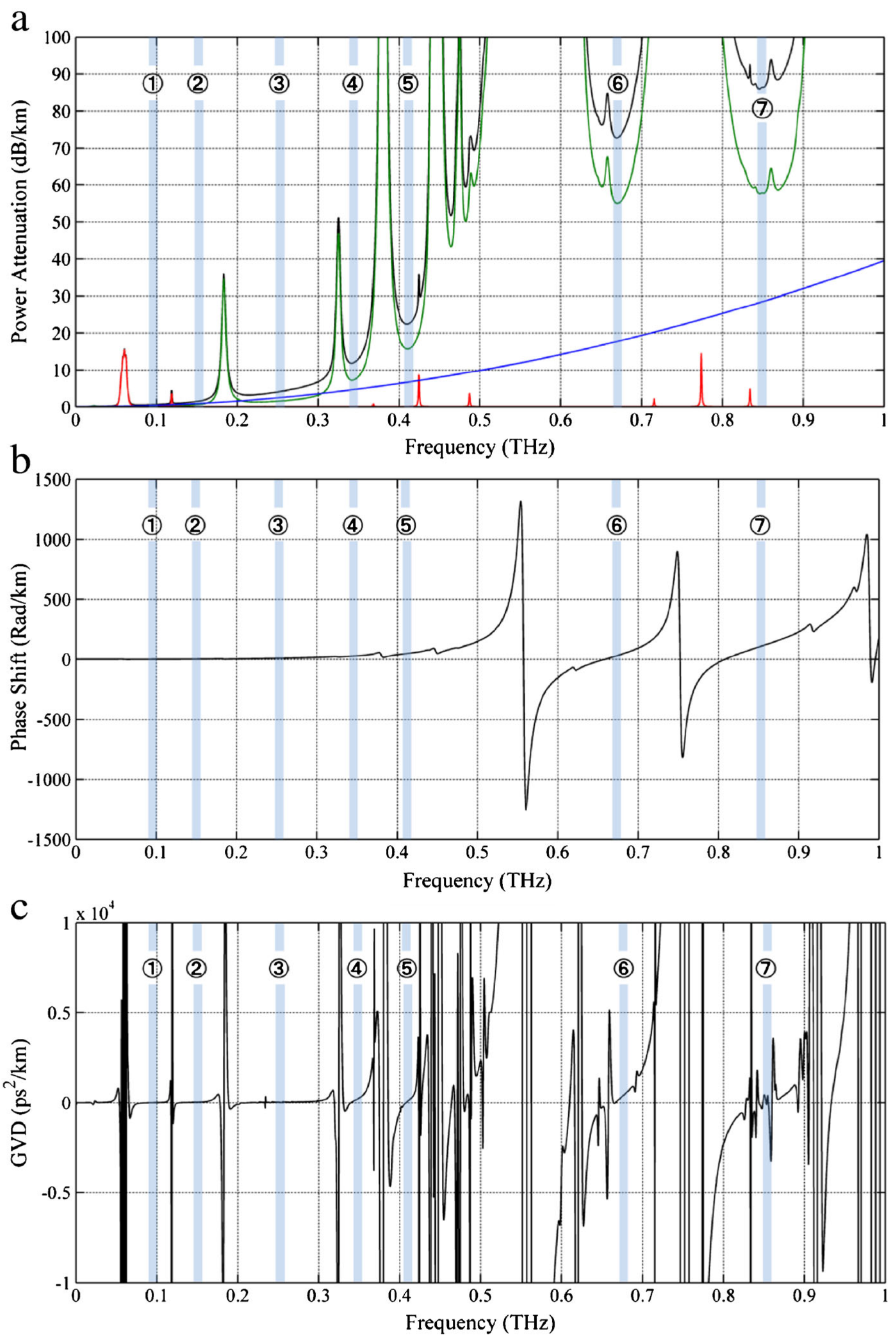

**Fig. 9** Summary results for the atmosphere at RH 58% and 20 °C (density of 10 g/m$^3$). The numbered shaded lines mark the digital communication channels at 96 GHz, 144 GHz, 252 GHz, 342 GHz, 408 GHz, 672 GHz, and 852 GHz. (a) The MRT + the continuum absorption + Oxygen absorption is shown as the upper black curve in units of dB/km. The MRT absorption is shown as the lower green curve. The continuum absorption is shown as the lowest blue curve. The oxygen absorption lines are shown as the lowest (red) resonance lines. (b) The vV-W-HITRAN + Oxygen phase in units of Radians/km. (c). The corresponding group velocity dispersion (GVD) in units of (ps$^2$/km)

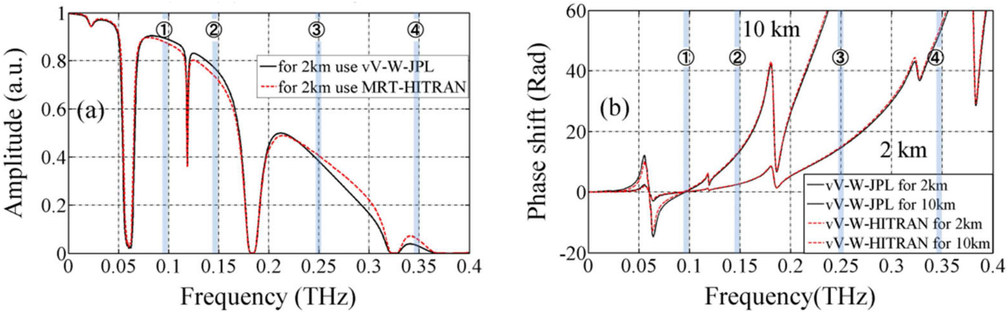

**Fig. 10** (a) Calculated amplitude transmission for a 2 km length of water vapor at RH 58% (10g/m$^3$) and 20°C and $O_2$ vapor in the atmosphere, for the MRT lineshape. The calculation also includes the water continuum absorption. (b) Corresponding calculated vV-W-HITRAN phase Φ in radians. For Channels 1-3, the calculated phase Φ is also shown for a 10 km length. The numbered shaded lines mark the digital channels at 96 GHz, 144 GHz, 252 GHz, and 342 GHz

The GVD results are presented in Fig. 9c, and Fig. 11 for the range from 0 to 400 GHz, and in Fig. 12 for the range from 400 to 1000 GHz. The GVD values are given in the standard optical fiber units of ps$^2$/km. The seven highlighted bands are located in regions of relatively small and stable GVD. The band frequencies and their GVD values in parenthesis are: 96 GHz (2.44 ps$^2$/km), 144 GHz (21.6 ps$^2$/km), 250 GHz (29.7 ps$^2$/km), 342 GHz (55.2 ps$^2$/km), 408 GHz

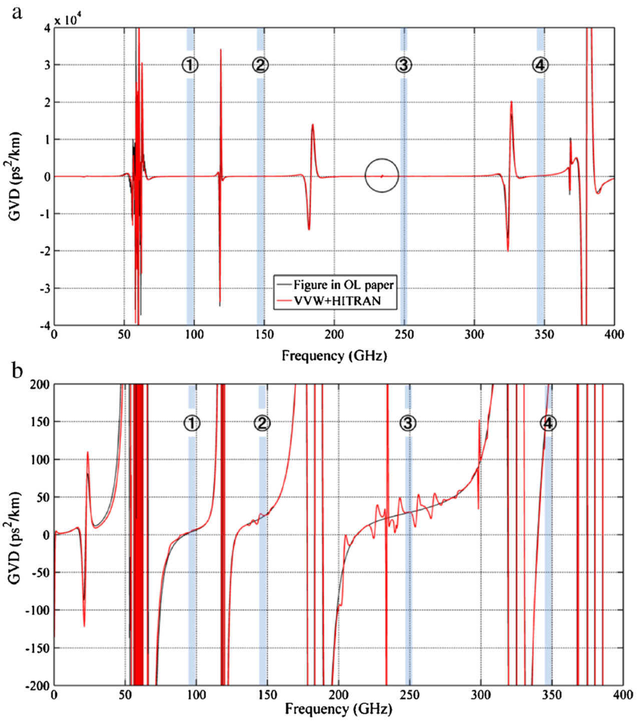

**Fig. 11** (a) GVD in ps$^2$/km from the phase results of Figs. 9b and 10b. (b) GVD results of (a) with a factor of 200 increase in vertical sensitivity show GVD = 2.44 ps$^2$/km at 96 GHz, GVD = 21.6 at 144 GHz, GVD = 29.7 at 250 GHz, and GVD = 55.2 at 342 GHz. The numbered shaded lines mark the digital communication channels at 96 GHz, 144 GHz, 252 GHz, and 342 GHz

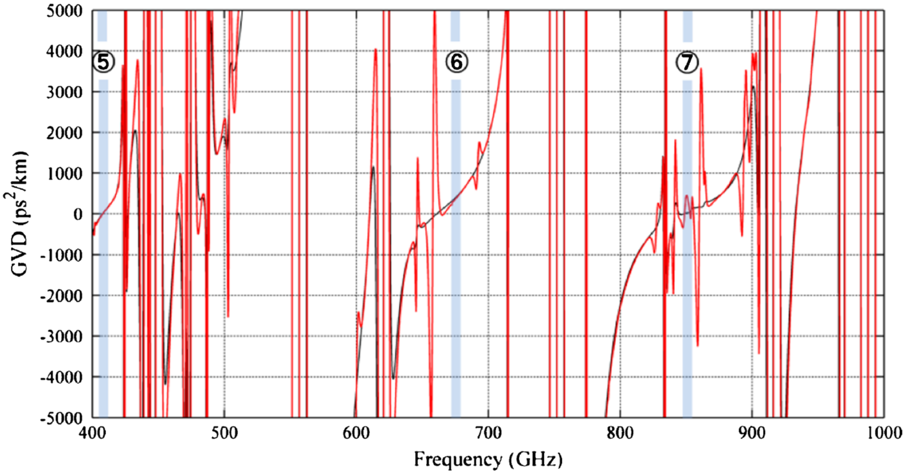

**Fig. 12** GVD obtained from Figs. 9b, and 9c, and shown from 400 to 1000 GHz. GVD = 0.37 ps$^2$/km at 408 GHz, GVD = 216 at 672 GHz, GVD = 190 at 852 GHz, The numbered shaded lines mark the digital communication channels at 408 GHz, 672 GHz, and 852 GHz

(0.37 ps$^2$/km), 672 GHz (216 ps$^2$/km), 852GHz (190 ps$^2$/km). The importance of these center frequencies will be shown in the simulated pulse propagation results.

Figure 11 shows good agreement between the new vV-W-HITRAN calculation (red detailed line) and the earlier vV-W-JPL calculation (black line) [40], except for the weak line within the circle at 235 GHz. For the expanded vertical scale of Fig. 11b, this weak water line appears as the very sharp response at 235 THz. In addition, there is new fine structure on the GVD curve in the neighborhood of 150 GHz and 250 GHz with the appearance of a small sharp line response near 300 GHz.

## 5 Long-Path, Good Bit-rate, Simulations of the Seven Communication Channels

The propagated THz pulses are obtained from a linear dispersion theory calculation in the frequency domain [21], using the absorption and phase displayed in Fig. 9, as shown below.

$$\mathbf{E}(\mathbf{z},\boldsymbol{\omega}) = \mathbf{E}(\mathbf{0},\boldsymbol{\omega})\mathbf{exp}[\mathbf{i}\boldsymbol{\Delta}\mathbf{k}(\boldsymbol{\omega})\mathbf{z}]\mathbf{exp}[-\boldsymbol{\alpha}(\boldsymbol{\omega})\mathbf{z}/\mathbf{2}], \tag{7}$$

for which the input complex amplitude spectrum is given by E(0,ω), and the output complex spectrum is given by E(z,ω). The phase is $\Phi = \Delta k(\omega)z$, and the amplitude transmission is exp[-α(ω)z/2]. The resulting time-domain pulses are IFFT of E(z,ω).

The simulation of the seven communication channels with center frequencies of 96 GHz, 144 GHz, 252 GHz, 342 GHz, 408 GHz, 672 GHz, and 852 GHz, uses the more physically correct MRT-HITRAN [27–29], for the absorption calculation and vV-W- HITRAN for the phase calculation, instead of vV-W-JPL, previously used for both [21, 40]. The HITRAN data base has significantly more tabulated water lines than the JPL data base, and HITRAN also calculates the individual linewidths of the water lines. The HITRAN data base is also used for oxygen, which mainly has a cluster of approximately 25 overlapping relatively strong lines at 60 GHz with FWHM linewidths of 1.2 GHz, a single weak $O_2$ line at 120 GHz, and a weak three line repetitive structure approximately every 350 GHz extending to well beyond 2 THz [41, 42].

The following simulations for the seven channels perform the propagation calculations for three transform-limited THz "one" bit pulses comprising the bit sequence of (1101), before and after passage through the atmosphere with RH 57.8% (10g/m$^3$) and 20 °C for a path length chosen to attenuate the channel by 10 dB. The coherent bit pulses are separated by an integral number of cycles of the center frequency. The symmetry of the input pulses shows that they are transform-limited with their envelopes determined by the ideal raised cosine spectrum [43], centered on the indicated carrier frequency. Their corresponding FWHM bandwidths (BW) are also indicated. These coherent bit pulses are also changed to current pulses by simulating homodyne detection with the local oscillator (LO) frequency equal to the carrier frequency and with a power detector. The calculated current bit pulses are obtained from the homodyne low frequency component centered on zero frequency. The resulting "one" bit pulses are ideal for digital electronics, as shown by their well resolved (1101) bit sequence.

In the Figures, due to absorption, the amplitudes of all the output pulses have been multiplied by the factor of 2 in order to increase their visibility, compared to the input pulses,. Taking this factor into account an approximate absorption for the output pulses can be obtained from the figures by taking the square of the ratio of the output pulse amplitude to the input pulse. This simple calculation gives absorptions of 1 or 2 dB higher than the expected 10 dB, which is explained by the output pulse broadening and BW broader than the channels minimum absorption region. As will be shown in Figs. 14 and 15, pulse broadening can be minimized by locating the center frequency at the GVD minimum within the channel and limiting the bandwidth to the region of acceptable GVD.

A propagation calculation for three transform-limited, 96 GHz Channel 1 (Channel-I [40]) THz "one" bit pulses is shown in Fig. 13a, before and after passage through 17.5 km of atmosphere with water vapor at RH 58% and 20 °C (10g/m$^3$). The FWHM bandwidth is 30 GHz. The bit separation is 9 LO periods equal to 93.75 ps, corresponding to the bit rate of 10.7 Gb/s.

A propagation calculation for three transform-limited, 144 GHz, Channel 2, THz "one" bit pulses is shown in Fig. 14a, before and after passage through 7.4 km of atmosphere with (10g/m$^3$) water vapor. The bit separation is 12 LO periods equal to 83.88 ps, corresponding to 12.0 Gb/s. The

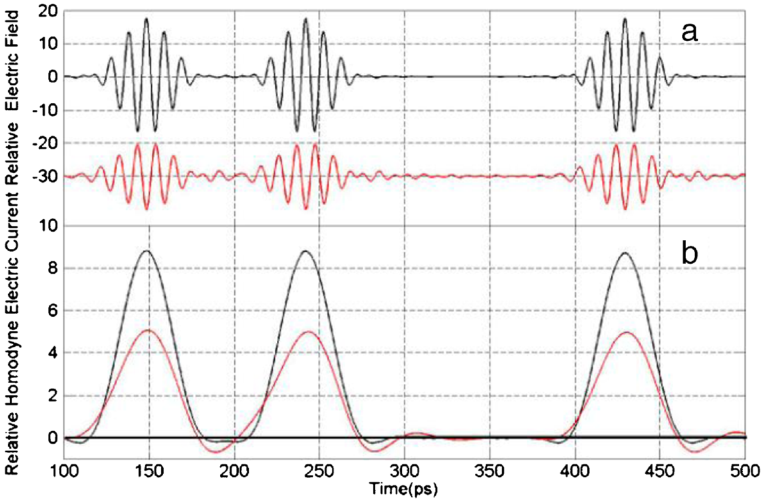

**Fig. 13** **Channel 1**. (a) 96 GHz, 10.7 Gb/s, 30 GHz BW (Channel-I [40]) input THz "one" bit pulses (black larger pulses) and calculated smaller, red (multiplied by 2) output pulses after 17.5 km propagation in the atmosphere with RH 58% (10g/m$^3$) and 20 °C. (b) Calculated homodyne input upper black current pulses and the output lower red (multiplied by 2) pulses, clearly showing the (1101) bit sequence

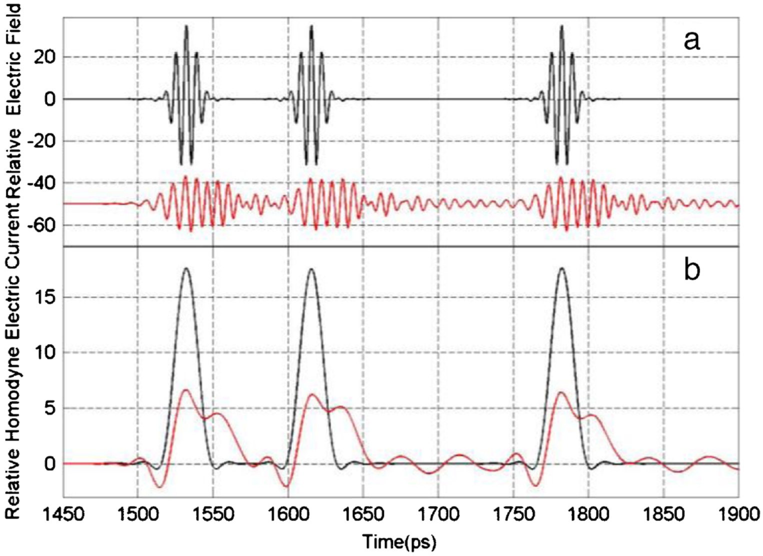

**Fig. 14** **Channel 2.** (a) 144 GHz, 12.0 Gb/s, 60 GHz BW, input THz "one" bit pulses (black larger pulses) and calculated red (multiplied by 2) lower attenuated output pulses after 7.4 km propagation in the atmosphere with RH 58% (10g/m$^3$) and 20 °C. (b) Calculated homodyne input upper black current pulses and the output lower red (multiplied by 2) pulses, showing an unacceptable four bit sequence (1101)

FWHM bandwidth is 60 GHz. As shown below, the Channel 2 pulses were unacceptably reshaped and broadened by GVD with propagation. To reduce this broadening the bandwidth was reduced to 30 GHz as shown in Fig. 15 with excellent results. The same propagation calculation for the above three, 144 GHz, FWHM bandwidth 30 GHz, Channel 2, THz "one" bit pulses is shown in Fig. 15a, before and after passage through 7.4 km of atmosphere.

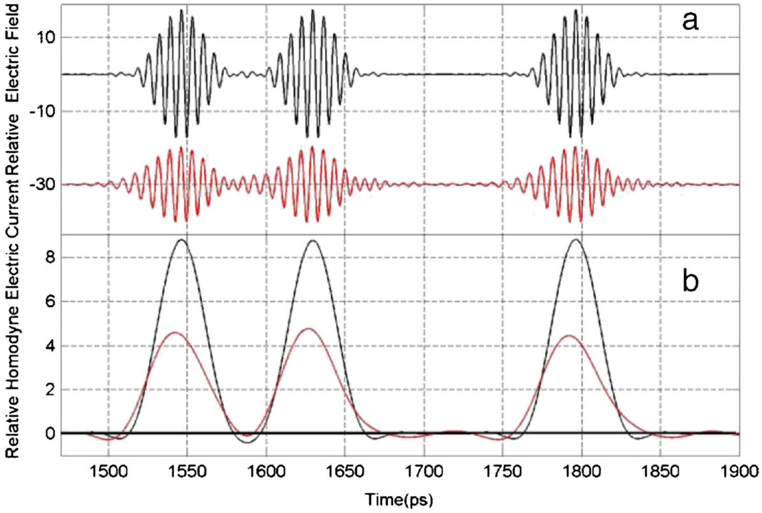

**Fig. 15** **Channel 2.** (a) 144 GHz, 12.0 Gb/s, 30 GHz BW, input THz "one" bit pulses (black upper larger pulses) and calculated red (multiplied by 2) lower attenuated output pulses after 7.4 km propagation in the atmosphere with RH 58% (10g/m$^3$) and 20 °C. (b) Calculated homodyne input upper black current pulses and the output lower red (multiplied by 2) pulses, clearly showing the four bit sequence (1101)

A propagation calculation for three transform-limited, 252 GHz Channel 3 (Channel-II [40]), THz "one" bit pulses is shown in Fig. 16a, before and after passage through 2.5 km of atmosphere with (10g/m$^3$) water vapor. The bit separation is 10 LO periods equal to 39.68 ps, corresponding 25.2 Gb/s. The FWHM bandwidth is 50 GHz.

A propagation calculation for three transform-limited, 342 GHz, Channel 4, THz "one" bit pulses is shown in Fig. 17a, before and after passage through 840 m of atmosphere with (10g/m$^3$) water vapor. The bit separation is 30 LO periods equal to 87.72 ps, corresponding 11.4 Gb/s. The FWHM bandwidth is 24 GHz.

A propagation calculation for three transform-limited, 408 GHz, Channel 5, THz "one" bit pulses is shown in Fig. 18a, before and after passage through 440 m of atmosphere with (10g/m$^3$) water vapor. The bit separation is 30 LO periods equal to 73.53 ps, corresponding to 13.6 Gb/s. The FWHM bandwidth is 30 GHz.

A propagation calculation for three transform-limited, 672 GHz, Channel 6 THz "one" bit pulses is shown in Fig. 19a, before and after passage through 140 m of atmosphere with (10g/m$^3$) water vapor. The bit separation is 30 LO periods equal to 44.64 ps, corresponding to 22.64 Gb/s. The FWHM bandwidth is 60 GHz.

A propagation calculation for three transform-limited, 852 GHz, Channel 7 THz "one" bit pulses is shown in Fig. 20a, before and after passage through 120 m of the atmosphere with (10g/m$^3$) water vapor. The bit separation is 30 LO periods equal to 35.21 ps, corresponding to 28.4 Gb/s. The FWHM bandwidth is 60 GHz.

## 6 Short Path, High Bit-Rate Simulations for 852 GHz Channel 7

We now present propagation simulations for digital data in Channel 7 at 852 GHz with a 108 GHz bandwidth, and bit-rates of 56.8 Gb/s for propagation distances of 10 m, 40 m, and 160 m. We also present simulations with bit-rates of 71.0 Gb/s for propagation distances of 10 m, 40 m, and 80 m.

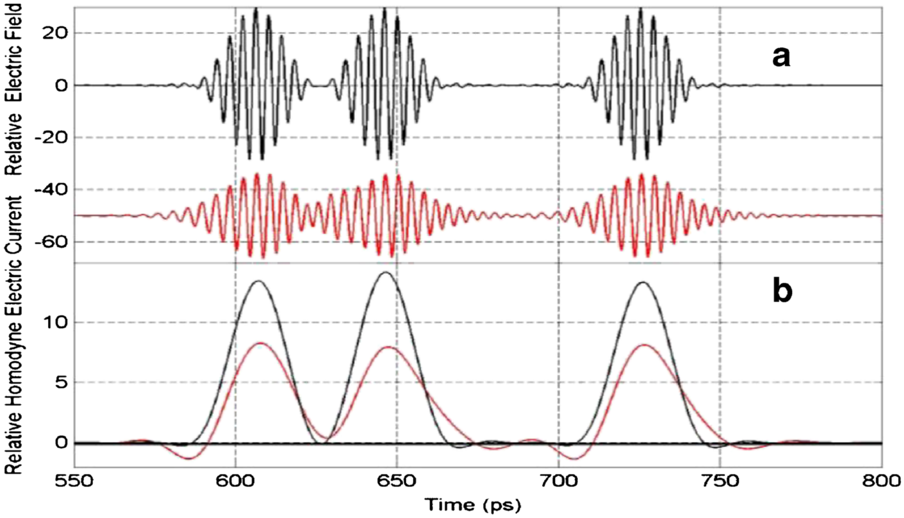

**Fig. 16** **Channel 3.** (a) 252 GHz, 25.2 Gb/s, 50 GHz BW, (Channel-II [38]), input THz "one" bit pulses (black larger pulses) and calculated red (multiplied by 2) output pulses after 2.5 km propagation in the atmosphere with RH 58% (10g/m$^3$) and 20 °C. (b) Calculated homodyne input upper black current pulses and the output lower red (multiplied by 2) pulses, showing the four bit sequence (1101)

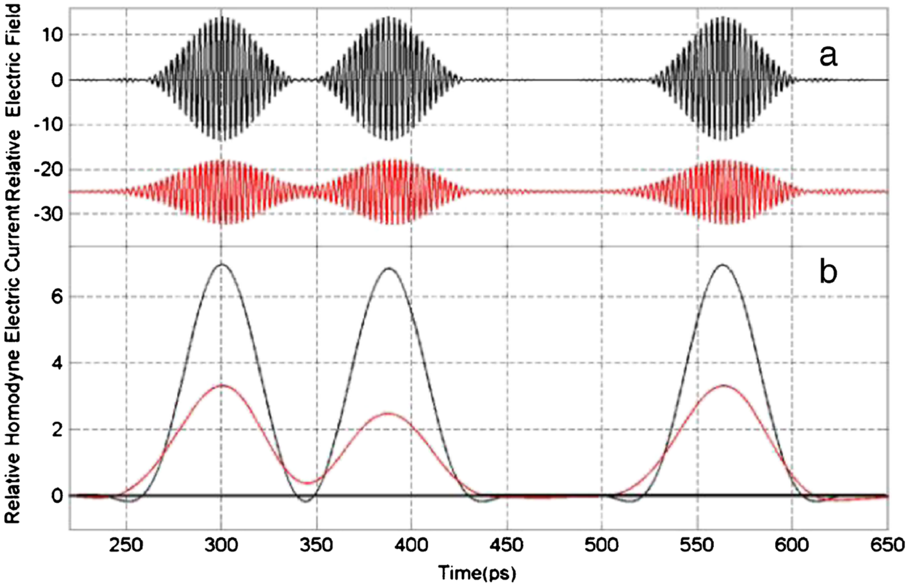

**Fig. 17** **Channel 4.** (a) 342 GHz, 11.4 Gb/s, 24 GHz BW, input THz "one" bit pulses (black upper larger pulses) and calculated red (multiplied by 2) lower attenuated output pulses after 840 m propagation in the atmosphere with RH 58% (10g/m$^3$) and 20 °C. (b) Calculated homodyne input upper black current pulses and the output lower red (multiplied by 2) pulses, showing the four bit sequence (1101)

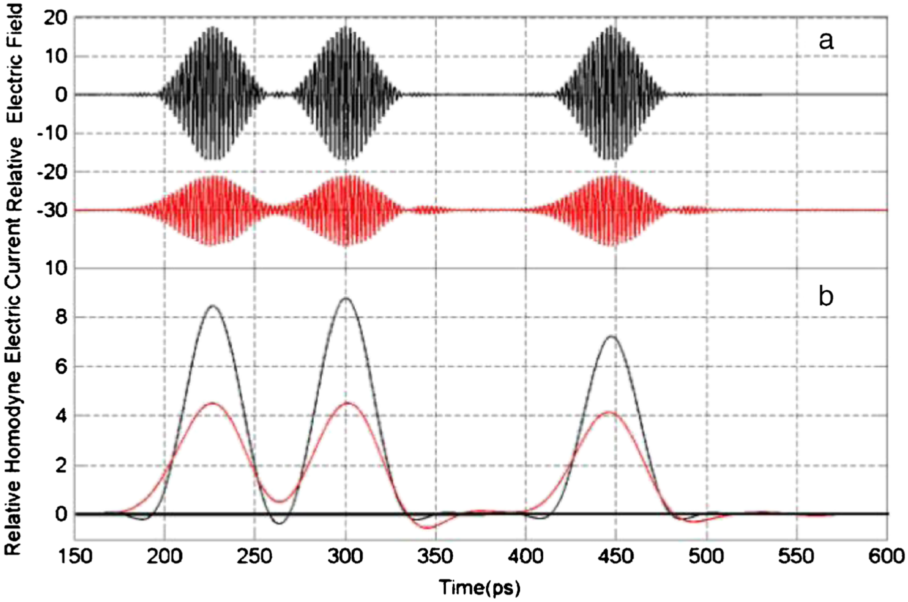

**Fig. 18** **Channel 5.** (a) 408 GHz, 13.6 Gb/s, 30 GHz BW, input THz "one" bit pulses (black upper larger pulses) and calculated red (multiplied by 2) lower attenuated output pulses after 440 m propagation in the atmosphere with RH 58% (10g/m$^3$) and 20 °C. (b) Calculated homodyne input upper black current pulses and the output lower red (multiplied by 2) pulses, showing the four bit sequence (1101)

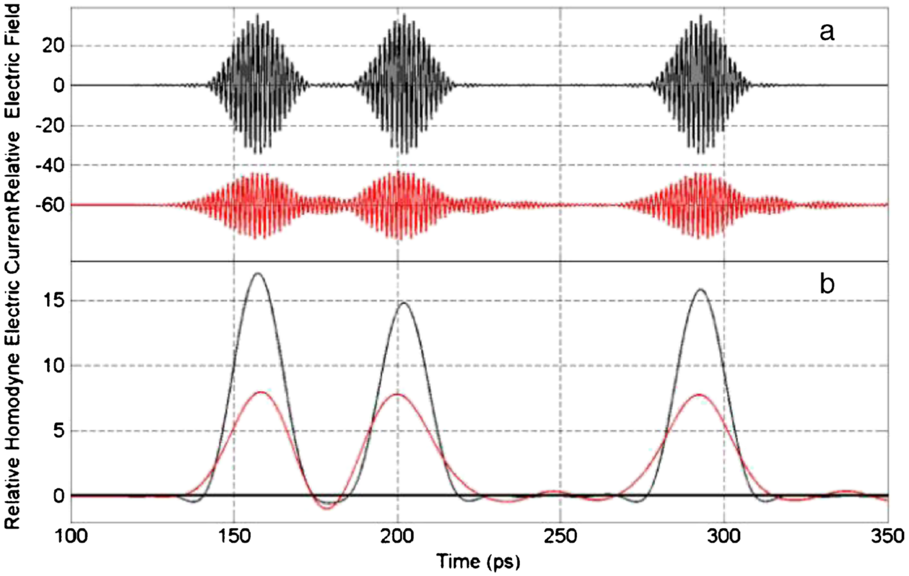

**Fig. 19 Channel 6.** (a) 672 GHz, 22.6 Gb/s, 60 GHz BW, input limited THz "one" bit pulses (black upper larger pulses) and calculated red (multiplied by 2) lower attenuated output pulses after 140 m propagation in the atmosphere with RH 58% (10g/$m^3$) and 20 °C. (b) Calculated homodyne input upper black current pulses and the output lower red (multiplied by 2) pulses, showing the four bit sequence (1101)

A propagation calculation for three transform-limited, 852 GHz, Channel 7 THz "one" bit pulses is shown in Figs. 21, 22 and 23, before and after passage through 10 m, 40 m, and 160

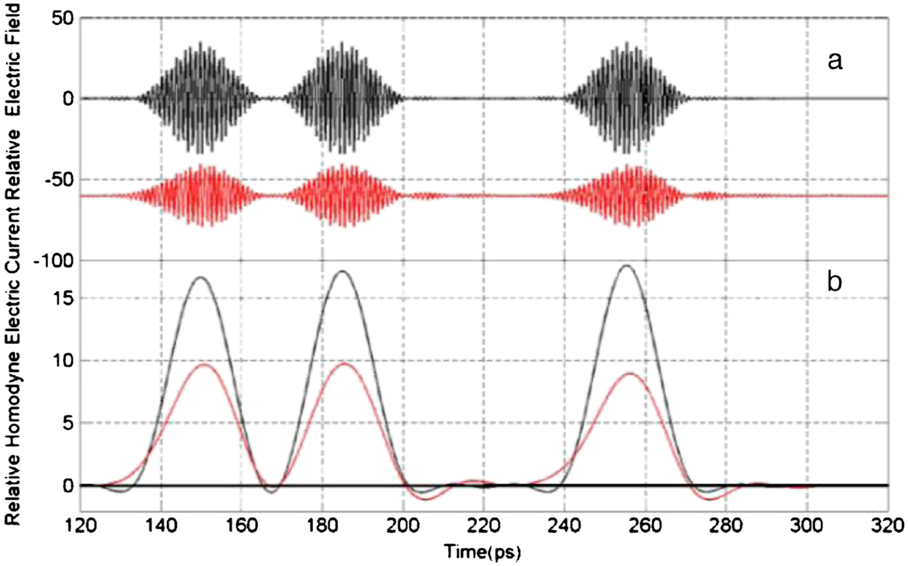

**Fig. 20 Channel 7.** (a) 852 GHz, 28.4 Gb/s, 60 GHz BW, input THz "one" bit pulses (black upper larger pulses) and calculated red (multiplied by 2) lower attenuated output pulses after 120 m propagation in the atmosphere with RH 58% and 20 °C. (b) Calculated homodyne input upper black current pulses and the output lower red (multiplied by 2) pulses, showing the four bit sequence (1101)

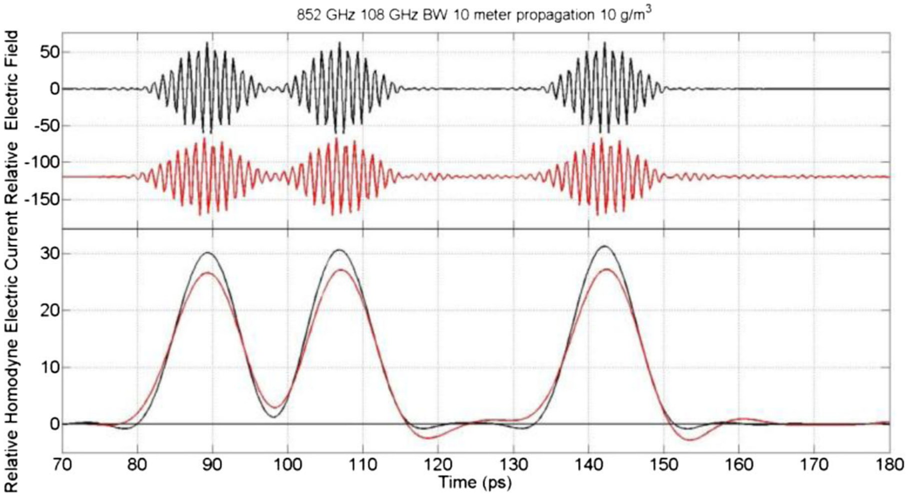

**Fig. 21** **Channel 7.** (a) 852 GHz, 56.8 Gb/s, 108 GHz BW, input THz "one" bit pulses (black upper larger pulses) and calculated red, lower, slightly-attenuated output pulses after 10 m propagation in the atmosphere with RH 58% and 20 °C. (b) Calculated homodyne input upper black current pulses and the output lower red pulses, showing the six bit sequence (011010)

m, respectively, of the atmosphere with (10g/m$^3$) water vapor. The bit separation is 15 LO periods equal to 17.61 ps, corresponding to 56.8 Gb/s. The FWHM bandwidth is 108 GHz.

A propagation calculation for three transform-limited, 852 GHz, Channel 7 THz "one" bit pulses is shown in Figs. 24, 25, and 26 before and after passage through 10 m, 40 m, and 80 m,

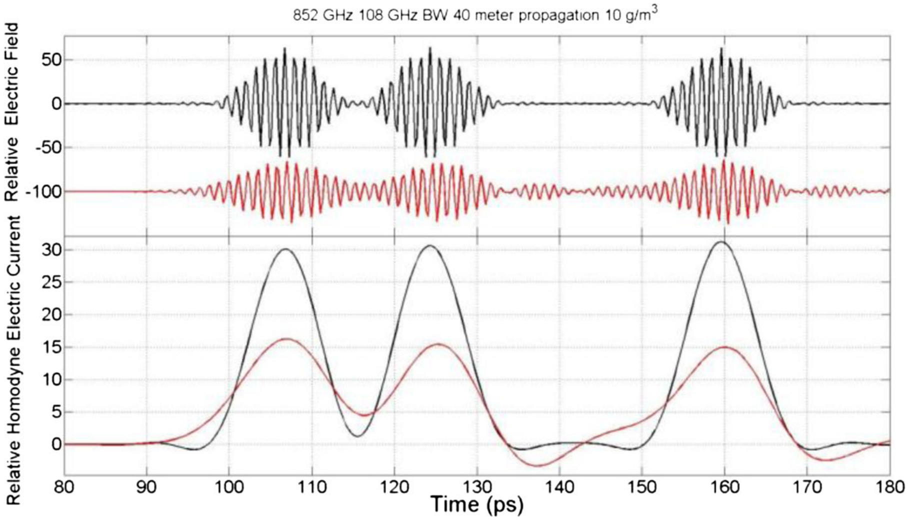

**Fig. 22** **Channel 7.** (a) 852 GHz, 56.8 Gb/s, 108 GHz BW, input THz "one" bit pulses (black upper larger pulses) and calculated red lower attenuated output pulses after 40 m propagation in the atmosphere with RH 58% and 20 °C. (b) Calculated homodyne input upper black current pulses and the output lower red pulses, showing the six bit sequence (011010)

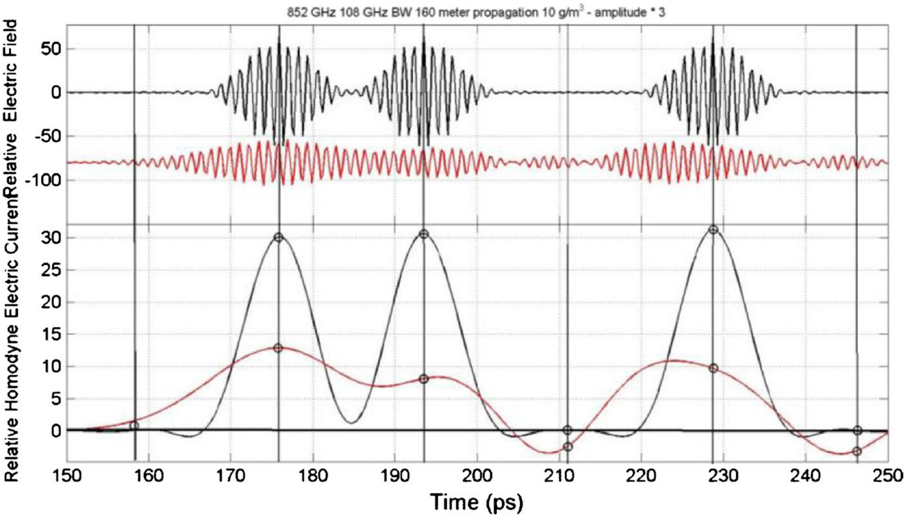

**Fig. 23** **Channel 7.** (a) 852 GHz, 56.8 Gb/s, 108 GHz BW, input THz "one" bit pulses (black upper larger pulses) and calculated red (multiplied by 3) lower attenuated output pulses after 160 m propagation in the atmosphere with RH 58% and 20 °C. (b) Calculated homodyne input upper black current pulses and the output lower red (multiplied by 3) pulses, showing the six bit sequence (011010). The six black vertical lines mark the center of the bit slots. The decision point values are marked by the black circles

respectively, of the atmosphere with (10g/m$^3$) water vapor. The bit separation is 12 LO periods equal to 14.08 ps, corresponding to 71.0 Gb/s. The FWHM bandwidth is 108 GHz.

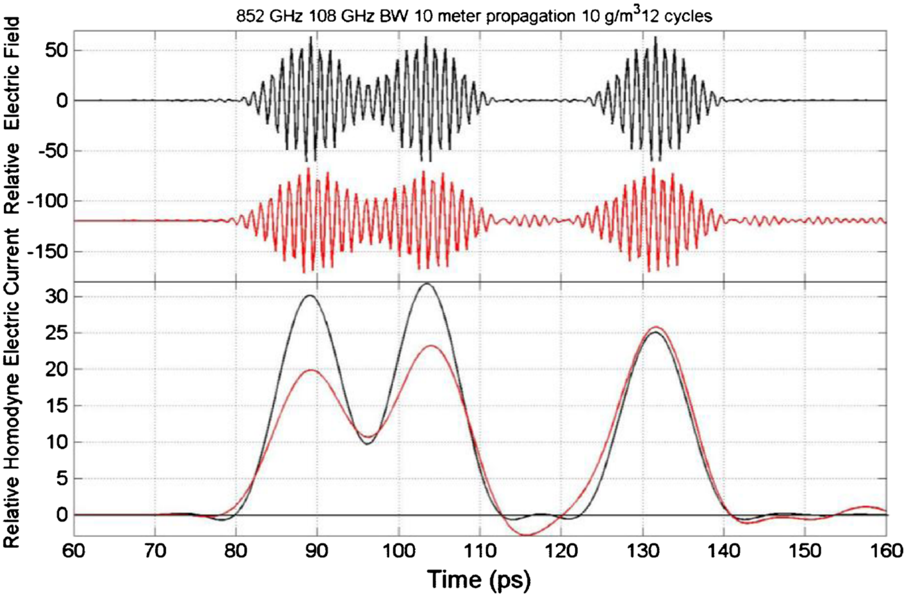

**Figure 24** **Channel 7.** (a) 852 GHz, 71.0 Gb/s, 108 GHz BW, input THz "one" bit pulses (black upper larger pulses) and calculated red lower output pulses after 10 m propagation in the atmosphere with RH 58% and 20 °C. (b) Calculated homodyne input upper black current pulses and the output lower red pulses, showing the six bit sequence (011010)

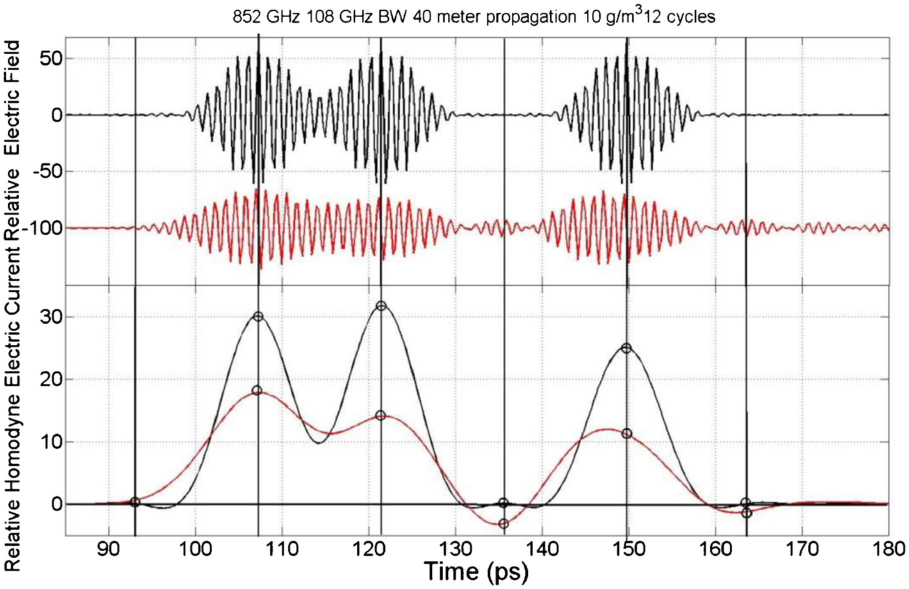

**Fig. 25** **Channel 7.** (a) 852 GHz, 71.0 Gb/s, 108 GHz BW, input THz "one" bit pulses (black upper larger pulses) and calculated red lower attenuated output pulses after 40 m propagation in the atmosphere with RH 58% and 20 °C. (b) Calculated homodyne input upper black current pulses and the output lower red pulses, showing the six bit sequence (011010). The six black vertical lines mark the center of the bit slots. The decision point values are marked by the black circles

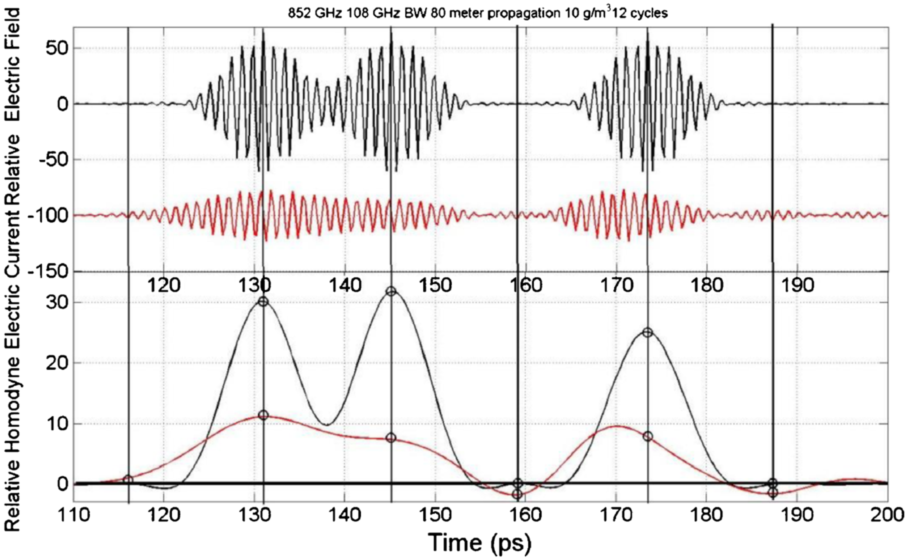

**Fig. 26** **Channel 7.** (a) 852 GHz, 71/0 Gb/s, 108 GHz BW, input THz "one" bit pulses (black upper larger pulses) and calculated red lower attenuated output pulses after 80 m propagation in the atmosphere with RH 58% and 20 °C. (b) Calculated homodyne input upper black current pulses and the output lower red pulses, showing the six bit sequence (011010). The decision point values are marked by the black circles

## 7 Quasi-Optic Analysis of Antenna Coupling

Quasi-Optics refers to the use of optical concepts, systems and components for frequencies with wavelengths as large as 1/4 the size of the lenses and focusing mirrors. For example, silicon hyper-hemispherical silicon lenses with a diameter of 10 mm and a 5 mm radius of curvature were shown to provide good THz coupling, into 240 μm diameter cylindrical metal tubes (waveguides) from the cut-off frequency at 0.65 THz to 3.5 THz [44]. Using cylindrical Si lenses with a curvature of 5 mm, excellent TEM coupling, into a parallel plate metal waveguide with a 108 μm plate separation, was demonstrated from 0.1 to 4.5 THz [45]. For these observations 12.5 cm focus, 75 mm diameter, 90 degree paraboloidal metal coated focusing mirrors were used. Basically, all THz transparent optical components can be used. Metal coated flat and focusing optical mirrors give excellent performance for THz and mm-waves.

Here we bring together optical, THz, mm-wave and microwave concepts, by showing that the Friis Transmission Equation [46, 47] given below is identical to the intuitive quasi-optic understanding of antenna coupling [48].

$$(P_R/P_T) = G_T G_R[\lambda/(4\pi R)]^2 \tag{8}$$

$P_T$ is the power to the no-loss transmitting antenna and $P_R$ is the power delivered to the receiving antenna. $G_T$ and $G_R$ are the antenna gains for the transmitter and receiver with respect to the isotropic radiator; λ is the wavelength and R is the distance between the two antennas. The antenna gain is given by the ratio of the 4π solid angle of the sphere to the solid angle defined by the propagating beam of the antenna [48]. The gain is equivalent to the surface area of the sphere divided by the area illuminated on the sphere by the propagating beam with the Gaussian amplitude diameter $D_{TR}$ at the distance R

$$G_T = \left(4\pi R^2\right)/\left(0.25\pi D_{TR}{}^2\right) \tag{9}$$

For a Gaussian beam emitted by the transmitting antenna with diameter $D_T$, the amplitude diameter at distance R is given by

$$D_{TR} = 4R\lambda/(\pi D_T) \tag{10}$$

Equations (9) and (10) have the same form for the receiver, for which $D_{TR}$ is replaced by $D_{RR.}$ Using these substitutions and replacing $G_T$ and $G_R$ with Eq. (9) and the equivalent for $G_R$ with $D_{RR,}$ Eq. (8) becomes

$$(P_R/P_T) = (D_R/D_{TR})^2 \tag{11}$$

Equation (11) shows the intuitive result, that ($P_R$ / $P_T$) is simply the ratio of the area of the receiver antenna to the area of the transmitted beam at the distance R. In the following presentation of applications, we will discuss antenna coupling in terms of $D_{TR}$ and $D_R$. With respect to the power transfer of the incident Gaussian beam through the circular aperture of the receiving antenna, we note that 86% of the incoming power is contained within the amplitude diameter $D_{TR}$ [49], and that usually $D_R << D_{TR}$.

Equation (10) is for R in the far-field Fraunhofer region, where the angular variation of the diffraction pattern is constant. A more general result, which includes R values in the near-field is given by

$$D_{TR} = D_T\left[1 + (R/R_R)^2\right]^{1/2}, \tag{12}$$

where $R_R$ is the Rayleigh range [49]. and is given by

$$R_R = \pi(D_T/2)^2/\lambda. \tag{13}$$

Equation (12) is valid for short paths and goes smoothly into the stable Fraunhofer region as R is increased.

In order to later discuss a variety of applications, for which a wide range of propagation distances are needed, Table I shows the calculated Rayleigh ranges $R_R$ for THz Gaussian beams with different initial diameters $D_T$ for the seven Communication Channels. For a propagation distance equal to the Rayleigh range the amplitude beam diameter of the Gaussian transmitter beam has increased by the square root of two, as shown by Eq. (12).

## 8 Fog, Rain and Scintillations

The effect of rain on direct THz links is approximately shown in the comprehensive Fig. 2 for 4 mm/hr. The attenuation of such a 4 mm/hr rain is also shown in Fig. 27, for a calculation based on the ITU-R-Model-2005 [50]. From an examination of the figure it can be seen, that for the seven channels described in this paper, we can use the conservative upper value of 4 dB/km to determine the new 10 dB attenuation lengths for all of the channels in the presence of 4 mm/hr rain. This simple approach adds 4 dB/km to the entire absorption plot shown in Fig. 9a. The resulting new pathlengths in the rain for a total of 10 dB attenuation are the following: Channel 1: 96 GHz (2.2 km), Channel 2: 144 GHz (1.9 km), Channel 3: 252 GHz (1.3 km), Channel 4: 342 GHz (630 m), Channel 5: 408 GHz (375 m), Channel 6: at 672 GHz (133 m), and Channel 7: 852 GHz (115 m).

The attenuation of fog at 20°C and RH 44%, for the seven links is also shown in Fig. 2, for a visibility of 100 m. The attenuation of fog with a visibility of 50 m and a density of 0.1 g/m$^3$ is approximately 0.4 dB at 100 GHz and monotonically rises to the constant value of 4 dB/km for a plateau starting at 700 GHz and extending past 1000 GHz [51]. This dependence gives the additional fog only attenuation for our seven channels of 0.4 dB/km, 0.6 dB/km, 1.3 dB/km, 1,8 dB/km, 2.2 dB/km, 4.0 dB/km, and 4.0 dB/km, at 96, 142, 252, 342, 408, 672, and 852 GHz, respectively. This simple approach adds these values to the attenuations for the channels shown in Fig. 9a. The resulting new fog pathlengths with 10 dB attenuation are the

**Table I** Calculated Reyleigh range $R_R$ for THz transmitter beams with different initial diameters $D_T$ for the Communication Channels.

| Channel<br>**$D_T$** | 1<br>96 GHz<br>3.13 mm | 2<br>144 GHz<br>2.08 mm | 3<br>252 GHz<br>1.19 mm | 4<br>342 GHz<br>877 μm | 5<br>408 GHz<br>735 μm | 6<br>672 GHz<br>446 μm | 7<br>852 GHz<br>352 μm |
|---|---|---|---|---|---|---|---|
| 50 cm | 62.8 m | 94.2 m | 165 m | 224 m | 267 m | 440 m | 558 m |
| 25 cm | 15.7 m | 23.6 m | 41.3 m | 56.0 m | 66.8 m | 110 m | 139 m |
| 10 cm | 2.51 m | 3.77 m | 6.60 m | 8.96 m | 10.7 m | 17.6 m | 22.3 m |
| 5 cm | 62.8 cm | 94.3 cm | 1.65 m | 2.24 m | 2.67 m | 4.40 m | 5.58 m |
| 2.5 cm | 15.7 cm | 23.6 cm | 41.3 cm | 56.0 cm | 66.8 cm | 1.10 m | 1.40 m |
| 1 cm | x | 3.78 cm | 6.61 cm | 8.96 cm | 10.7 cm | 17.6 cm | 22.4 cm |
| 5 mm | x | x | 1.65 cm | 2.23 cm | 2.67 cm | 4.39 cm | 5.57 cm |

X indicates too few wavelengths for the quasi-optic solution.

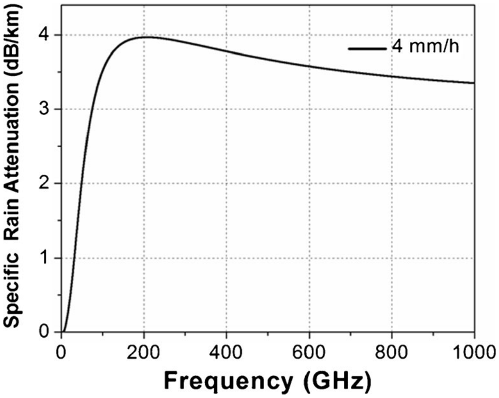

**Fig. 27** Calculation of attenuation due to 4 mm/hr rain

following: **Channel 1**: 96 GHz (10.3 km), **Channel 2**: 144 GHz (5.1 km), **Channel 3:** 252 GHz (1.9 km), **Channel 4:** 342 GHz (730 m), **Channel 5**: 408 GHz (400 m), **Channel 6: at** 672 GHz (130 m), and **Channel 7**: 852 GHz (110 m).

However, if such a fog is associated with the humidity rising to RH 100%, the attenuation of the 7 channels shown in Fig. 9a would need to be increased by the factor 100/58 = 1.72, these values added to the fog only attenuations given above. For these large attenuations due to the fog only plus the increase due to the associated 100% humidity, the corresponding 10 dB attenuation, channel lengths are the following: **Channel 1**: 96 GHz (7.2 km), **Channel 2**: 144 GHz (3.4 km), **Channel 3:** 252 GHz (1.2 km), **Channel 4:** 342 GHz (450 m), **Channel 5**: 408 GHz (240 m), **Channel 6: at** 672 GHz (80 m), and **Channel 7**: 852 GHz (70 m). Such a situation will lead to signal reductions of more than 10 dB.

For the direct long-path links, it might be expected that scintillations, time varying fluctuations in the refractivity, due to atmospheric temperature and humidity variations, would lead to phase distortions of the transmitted coherent THz pulses and consequent changes in the incoming beam direction. The effect of such turbulence on propagating electromagnetic radiation has been predicted theoretically [52], and verified experimentally for propagating IR and optical radiation [53], that the log amplitude variance of amplitude fluctuations due to atmospheric turbulence varies as $\mathbf{(f)^{7/6}}$ , with f = frequency. Consequently, it was quite surprising that the observed mm-wave turbulence effects were more than 2 orders of magnitude larger than expected. This is due to the comparatively very large and frequency independent refractivity of water vapor from microwave frequencies to beyond 1000 GHz [37, 54]. Within this range, the scintillation effecr is expected to increase with an essentially linear frequency dependence. An experiment measuring intensity and angle of arrival (AOA) effects has been done with a 140 GHz beam over pathlengths of 1.3 km. Also, for a longer 25 km path with a 173 GHz beam, using an interferometric radar system capable of measuring deviations of micro-radians, an AOA distribution with standard deviation of only 10 micro-radians was observed [55]. This angular distribution is considerably smaller than the full angular beam divergence of 1.4 mrad (1,400 micro-radians) for the proposed 17.5 km, 96 GHz digital communications link with 2 m diameter antennas and for the proposed 252 GHz LEO satellite link with a full angular beam divergence of 100 micro-radians. Consequently, for our proposed longer links scintillation does not appear to be a problem, even though for higher frequencies the problem becomes more severe.

## 9 Long-Path, Good Bit-Rate, Applications

Consider a THz ground link transmitter with a 2 m dish antennas operating at 96 GHz would have the diffraction-limited beam amplitude power diameter of 35.2 m at 17.5 km. The power transfer between the two 2 m antennas is given by the ratio of the area of the 2 m receiving antenna to that of the diffraction limited beam $(2\text{ m}/ 35.2\text{ m})^2 = 3.23 \times 10^{-3}$, corresponding to the diffraction propagation loss of 24.9 dB. The full angular beam power divergence is 2.0 mrad, compared to the human eye with a resolution angle 0.29 mrad. Consequently, an optical sight could enable the initial alignment between the two antennas. A telescopic sight aligned to the transmitting antenna, would facilitate precise alignment.

Another important consideration for the point-to-point 17.5 km link is effect of the curvature of the earth. Compared to a flat surface, the curvature of the earth, drops the receiver by the significant distance of 24.0 m. This will have to be compensated for by surface elevation differences or tower heights.

Although THz waves have higher attenuation than microwaves from a humid atmosphere, rain, fog, dust and scintillations, THz waves are much better than the Free Space Optical (FSO) communication systems, which use infrared and optics, under the same weather conditions. Moreover, the FSO has limitations on the data rates and transmission distance, from eye-safety limited transmission power, and the misalignment between transmitter and receiver. The THz wireless communication system is an alternative option to replace FSO with a more robust operation in bad weather.

An important demonstration of a custom built NTT prototype wireless system [3], was the 800 m wireless transmission trial of live television broadcast coverage of the Beijing 2008 Olympics [3]. The transmitted power of 10 mW of 120 GHz Band 10 GbB (10.3125 Gb/s), had simple amplitude shift keying, and the receiver sensitivity was -35 dBm for a bit error rate of less than $10^{-12}$ [3].

The NTT system would be capable of driving the proposed 17.5 km link, using 2 m dish antennas, but with a change to the optimal carrier frequency of 96 GHz for lower absorption and minimal GVD. The total of the atmospheric loss of 10 dB and the diffraction loss of 25 dB for our 17.5 km link is 35 dB, giving the proposed system a power margin of 10 dB.

Another significant application to consider would be a 252 GHz THz link to a geosynchronous communications satellite approximately 35,800 km above sea level has several important features compared to existing satellite links. Using a 5 m diameter antenna for the earth gateway antenna, the diffraction-limited beam amplitude diameter at the satellite would be only 3.63 km. The power transfer between the 5 m ground antenna and the 2 m satellite antenna is given by the ratio of the area of the 2 m receiving antenna to that of the diffraction limited beam $(2\text{ m}/3.63\text{ km})^2 = 0.30 \times 10^{-6}$, corresponding to the diffraction propagation loss of only 65.2 dB, compared to 90 dB for a 10 GHz microwave system with a 20 m Gateway antenna and a 2 m satellite antenna. The full angular 252 GHz beam divergence is 0.10 mrad, requiring a pointing accuracy and stability 3 times better than the human eye. This stability is relatively easily obtained. A feature of this alignment precision is secure point-to-point communications.

It is important to note that the channel frequencies of 96 GHz, 144 GHz, and 252 GHz of this work are contained within the mm-wave domain, also designated as the extremely high frequency domain (EHF) extending from 30 to 300 GHz [5]. Our proposed Channel I, THz ground link with the center frequency of 96 GHz and 30 GHz FWHM bandwidth essentially fills the EHF-W Band with boundaries from 81-111 GHz [5]. Our Channel 3, THz geosynchronous satellite link with center frequency 252 GHz and 50 GHz FWHM bandwidth is also within the EHF domain.

At the present time no operative W-Band communication systems have been developed [3], and there is no commercial activity from W-Band up to 300 GHz, the high frequency limit of the EHF range. The W-Band is currently considered as the frontier for space telecommunications. There are several ongoing W-Band projects sponsored by the Italian Space Agency (ASI), Japan Aerospace Exploration Agency (JAXA), and NASA [5]. The program goals range from investigating the possibility of collecting data at 100 Mb/s with a BER of $10^{-11}$, and thereby enabling an upload to the on-board memory of at least 1 GB of data during the short time window of each passage over base stations [56]. Another program's goal is designing and developing a complete line of W-band communication satellite payloads [57]. A long term program is the development of the W-band Integrated Interplanetary Network to support future solar system exploration missions [58]. This system will consist of many data relay satellites positioned throughout the solar system.

## 10 Short Path, High Bit-Rate Applications

Advanced techniques, such as QAM, MIMO, Orthogonal Frequency Division Multiplexing (OFDM) can enhance THz wireless communication to even higher data rates. Recently, many investigations have been reported that focus on modern THz communication experiments, such as 2.5 Gbit/s Error-free links at 625 GHz for several meters [59], 25 Gbit/s MMIC-based link at 220 GHz for 10 m [60], and a 24 Gbit/s link at 300 GHz for 0.5 m [61]. Most recently, a 20 m direct digital link at 237.5 GHz with a bit rate of 100 Gb/s has been reported [62].

Here, we have shown, using as an example the highest frequency Channel 7 at 852 GHz with a 108 GHz bandwidth, that simple amplitude modulation can easily reach the data-rate of 56.8 Gb/s (corresponding to a 15 cycle bit separation) and propagate essentially undistorted for a 10 m path with insignificant absorption in the atmosphere at RH 58% and 20 °C (10g/$m^3$). A propagation of 40 m slightly distorts the pulses; the power absorption is 3.3 dB. A propagation of 160 m severely distorts and broadens the pulses, but the clean bit signal is maintained; the power absorption is 13.3 dB.

We have also shown using Channel 7 at 852 GHz and 108 GHz BW, that with a bit separation of 12 cycles, the bit-rate of 71.0 Gb/s is achieved and propagates for 10 m with only slight distortion and insignificant power absorption. A propagation of 40 m causes significant overlapping of adjacent pulses, but a clean bit-rate is maintained; the power absorption is 3.3 dB. A propagation of 80 m almost merges the adjacent pulses, but a clean bit rate is still maintained; the power absorption is 6.7 dB.

These simulations for the achievable bit-rates and our discussion of beam coupling, as summarized in Table I, provide a framework to present technical specifications for some of the short path high data rate applications. These applications have been listed and presented in Ref. [8], and discussed in various detail in the reviews [1–8]. Initially, we note that for all of our simulations, there is no pulse reshaping and insignificant absorption for pathlengths of less than 10 m. For such applications, the problems are to achieve a coupling between the transmitter and receiver with the coupling loss significantly less than the dynamic range of the system. We assume a dynamic range of 45 dB, that was demonstrated with the 10 Gb/s 800 m THz-link for the 2008 Olympic Games [3, 6, 7].

For the important application of Kiosk downloading [8], the THz transmitter is attached to the fixed download station, and makes a wireless connection of a few cm to accomplish an ultrahigh download of multimedia material to the mobile THz receiver of the customer. This application could be enabled by transceiver chips with standard 10 mm diameter Si lenses [44, 45] in optical contact to the chips. The generated 5 mm diameter beam of the 852 GHz signal would maintain its size for a 2 cm propagation path with essentially complete coupling to the similar 10 mm diameter lens on the receiver. This confocal situation is quite accommodating, and good coupling will occur for ± 0.5 mm alignment of the central axes of the lenses. However, the flat faces of the lenses in contact with the chips should be aligned parallel to ± 6 mrad. This requirement could be easily met with a standard mechanical alignment fixture. The reflection of the signal beam from the focusing lens of the receiver is not a problem, but the internal reflections from the transmitting lens could cause serious problems, which could be mitigated by anti-reflection coatings on the curved surfaces of both lenses.

For applications with a range of 10 m, THz wireless links are a promising solution for a wireless home entertainment system. The wireless solution for device connections is preferred, because it is portable, switchable and avoids tangling wires. However, at the present time only wireless speakers are commercialized due to the low data-rate required for the sound track. For the video signal stream, the compressed Blu-ray Disc video with a full 1080p High Definition (HD) picture runs at up to 40 Mb/s data rate, but to transmit an uncompressed Blu-ray video with the same resolution will require a data rate of 1.5 Gb/s to 3 Gb/s. Consequently, the Ultra High Definition (UHD) TV signals are now transmitted with various kinds of compression by HDMI cable between the storage devices (Blu-Ray, PC, Camcorder) and display (TV, projector) because currently available wireless links do not support ultra-fast data- rates.

The solution of the THz wireless link with center frequency of 852 GHz can use a typical transmitter with an output beam diameter of 1 cm. After 10 m transmission, the THz beam diameter has expanded from 1 cm to 90 cm. If the receiver diameter is 2.5 cm, the corresponding power coupling loss is 31 dB**,** which is less than the 45 dB dynamic range of the NTT receiver. For the distance of 10 m and stable indoor RH, the water vapor absorption can be neglected. To avoid the problem of people and moving objects blocking the THz beam connecting the TV and the distributed storage devices, a signal hub (or a reflector) could be mounted on the ceiling with a direct vertical THz link to the TV receiver. In addition, other distributed storage devices could set up links with this hub to transmit a HD signal stream to the TV, providing a geometry of multi-point to point switchable links. We note that the important problem of wall reflections has been studied in detail by ray-tracing simulations [1].

For applications with a range of 50 m, 852 GHz wireless links can provide a 70 Gb/s direct point-to point connection between computer clusters. In order to maintain the beam size and high point-to-point coupling efficiency, a transmitter with a 15 cm diameter output beam would produce a diffracted beam with a diameter of 19.6 cm, after a 50 m propagation. If the receiver has the same diameter as the transmitter, the power coupling loss would be only 2.3 dB. Extending the propagation to 100 m, the corresponding beam diameter will increase to 29.5 cm, with the corresponding coupling loss of 5.9 dB. The absorption loss is 8.3 dB for the 100 m propagation in the atmosphere with RH 58% and 20 °C. Metal coated flat and focusing mirrors, beam-splitters and large diameter plastic lenses are available for this application.

For a range of 100 m, the **852 GHz** wireless links are ideal to provide hotspots in a stadium, where large amounts of data are required by the crowds. If the signal generated from a 10 cm diameter transmitter and the average data transmission distance is 100 m, the 852 GHz beam will have expanded to 44.6 cm**.** The corresponding power coupling will be $(10/44.6)^2 = 5.0 \times 10^{-2}$, corresponding to 13 dB, plus the water vapor absorption loss of 8.3 dB for the 100 m propagation in the atmosphere with RH 58% and 20 °C.

With respect to the important need for the intermediate small cell and nanocell back-haul, that would be in place at near street level and would use the street signal light poles, large sign poles, and sturdy street light poles, for secure mounting, we point out the enabling features of the atmospheric THz link of Channel 7 at 852 GHz, BW 108 GHz, 56.8 Gb/s, which has a range of 160 m. Using 15 cm diameter transmitters and receivers, the 852 GHz beam diameter at 160 m would be 47.2 cm, giving a power coupling of $(15/47.2)^2 = 0.101$, equivalent to 10 dB coupling loss. This pattern would be easy to align using a light beam co-aligned and with the same divergence. The absorption loss would be 13.3 dB for the 160 m propagation in the atmosphere with RH 58% and 20 °C. Metal coated flat and focusing mirrors, beam-splitters and large diameter plastic lenses are available for this application.

For a longer THz back-haul from the inter-cell network, Channel 3 at 252 GHz, BW 102 GHz, 50.4 Gb/s, could be used. This channel would have a range of 1000 m, but would require larger optics, because of the wavelength increase of more than 3 times. Using 25 cm diameter transmitters and receivers, the 252 GHz beam diameter at 1000 m would be 606 cm, giving a power coupling of $(25/606)^2 = 0.00170$, equivalent to 27.7 dB coupling loss. At 500 m, the coupling loss would be 21.7 dB. Using 50 cm diameter transmitters and receivers, the 252 GHz beam diameter at 1000 m would be 307 cm, giving a power coupling of $(50/307)^2 = 0.0265$, equivalent to 15.8 dB coupling loss. This pattern would be easy to align optically. The absorption loss would be 4 dB for the 1000 m propagation in the atmosphere with RH 58% and 20 °C. These technical features can provide realistic parameters for future network design.

## 11 Conclusions

Combining recent measurements with the latest physical understanding of the atmosphere and using the extensive HITRAN data base, we have calculated, using linear dispersion theory, the propagation of THz bit pulses within the seven most promising THz atmospheric digital communication channels. The THz-wave digital communication channels have the following favorable features for a propagation loss of 10 dB at RH 58% and 20 °C (density of 10 $g/m^3$)): **Channel 1**: at 96 GHz, Bandwidth (BW) 30 GHz, 10.7 Gb/s for 17.5 km, **Channel 2**: at 144 GHz, BW 30 GHz, 12.0 Gb/s for 7.4 km, **Channel 3:** at 252 GHz, BW 50 GHz, 25.2 Gb/s for 2.5 km, **Channel 4:** at 342 GHz, BW 24 GHz, 11.4 Gb/s for 840 m, **Channel 5**: at 408 GHz, BW 30 GHz, 13.6 Gb/s for 440 m, **Channel 6: at** 672 GHz, BW 60 GHz, 22.6 Gb/s for 140 m, and **Channel 7**: at 852 GHz, BW 60 GHz, 28.4 Gb/s for 120 m.

The enabled long-path THz links were discussed. Two applications were presented in detail, namely, a long-path 17.5 km THz ground-link operating at 96 GHz, BW 30 GHz, 10.7 Gb/s, and a GEO satellite link at 252 GHz, BW 50 GHz, 25.2 Gb/s. In addition, Channel 7 at 852 GHz was studied by calculated pulse propagation to understand the relationships between higher bit-rates and propagation distance. It was shown that good digital transmission could be obtained with 852 GHz, BW 108 GHz, 56.8 Gb/s for a 160 m propagation distance in the atmosphere with RH 58% ($10g/m^3$) and 20 °C. Good digital transmission was also obtained with 852 GHz, BW 108 GHz, 71.0 Gb/s for 80 m. These results were discussed with respect to high bit-rate, short-path applications.

These channels with an optimum frequency and bandwidth to achieve minimum loss and minimum group velocity dispersion were chosen to optimize their performance to transmit digital data, without regard for frequency band boundaries and bandwidth allocations. Our results, which can enable many applications, have demonstrated the importance of the center frequency of wide-band allocations for optimized digital communications in the mm-wave and THz frequency range from 50 GHz to 1 THz, for which cross-talk is much reduced due the absorption of water vapor and to the line-of-sight nature of the mm-wave and THz links.

**Acknowledgment** This work was partially supported by the National Science Foundation.

## References

1. R. Piesiewicz, T. Kleine-Ostmann, N. Krumbholz, D. Mittleman, M. Koch, J. Schoebel, and T. Kurner, "Short-Range Ultra-Broadband Terahertz Communications: Concepts and Perspectives," IEEE Antennas and Propagation Magazine, **49**, No. 6, 24–39 (2007).
2. J. Wells, "Faster than Fiber: The Future of Multi-Gb/s Wireless," IEEE Microwave Magazine, May 2009, 104–112.
3. T. Kosugi, A. Hirata, T. Nagatsuma, and Y. Kado, "MM-Wave Long-Range Wireless Systems," IEEE Microwave Magazine, April 2009, 68–76.
4. J. Federici and L. Moeller, "Review of terahertz and subterahertz wireless communications," J. Appl. Phys. Vol. 107, 111101 (2010).
5. E. Cianca, T. Rossi, A. Yaholom, Y. Pinhasi, J. Farserotu, and C. Sacchi, "EHF for Satellite Communications: The New Broadband Frontier," Proceedings of the IEEE, **99,** 1858–1881 (2011).
6. T. Kleine-Ostmann and Tadao Nagatsuma, "A Review on Terahertz Communications Research," J. Infrared Milli Terahz Waves, **32**, 143–171 (2011).
7. Ho-Jin Song and Tadao Nagatsuma, " Present and Future of Terahertz Communications," IEEE Trans. THz Sci. Technol. **1**(1), 256–263 (2011).
8. T. Kurner, and S. Briebe, "Towards THz Communications – Status in Research, Standardization and Regulation," J. Infrared Milli TeraHz Waves **35**, 53–62 (2014).
9. D.E. Burch and D.A. Gryvnak, "Continuum Absorption by Water Vapor in the infrared and Millimeter Regions," in *Atmospheric Water Vapor,* A. Deepak, ed. (Academic Press, New York, NY 1980), pp. 47–76. Proceedings of the International Workshop on Atmospheric Water Vapor (Vail, Colorado, September 11–13, 1979).
10. Yu. A. Dryagin, A.G. Kislyakov, L.M. Kukin, A.I. Naumov and L.I. Fedosyev, Isvestya VUZ Radiosphsica, "Measurement of the Atmospheric Absorption of Radio Waves in the Range 1.36–3.0 mm," **9**, pp. 627–644, 1966.
11. R.L. Frenkel and D. Woods, "The Microwave Absorption by H2O and its Mixtures with Other Gases Between 100 and 300 Gc/s," Proc. IEEE, **54**, pp. 498–505, 1966.
12. A. W. Straiton and C. W. Tolbert, "Anomalies in the Absorption of Radio Waves by Atmospheric Gases," Proc. IRE, **48**, pp. 898–903, 1960.
13. V. Ya. Ryadov and N.I. Furashov, "Investigation of the spectrum of radiowave absorption by atmospheric water vapor in the 1.15 to 1.5 mm range," Radio Phys. and Quantum Electronics, **15**, pp. 1124–1128, 1974.
14. D. E. Burch, D.A. Gryvnak, and R.R. Patty, "Absorption of Infrared Radiation by CO2 and H2O: Experimental Techniques," J. Opt. Soc. Am. **57**, pp. 885–895, 1967.
15. D.E. Burch, "Absorption of Infrared Radiant Energy by CO2 and H2O. III. Absorption by H2O between 0.5 and 36 $\mathrm{cm}^{-1}$," J. Opt. Soc. Am. **58**, pp.1383–1394, 1968.
16. Y. Yang, A. Shutler and D. Grischkowsky, "Measurement of the Transmission of the Atmosphere from 0.2 to 2 THz," Opt. Express, **19**(9), 8830–8838 (2011).
17. S. Paine, R. Blundell, D. Papa, J. Barrett, and S. Radford, "A Fourier transform spectrometer for measurement of atmospheric transmission at submillimeter wavelengths," Publ astronom Soc Pacific, **112**(2), 108–126 (2000).
18. J. Melinger, Y. Yang, M. Mandehgar, and D. Grischkowsky, "THz detection of small molecule vapors in the atmospheric transmission windows," Opt. Express, **20**(6), 6788–6807 (2012).
19. P. H. Siegel, "Terahertz technology," IEEE Trans. Microwave Theory Tech., **50**, pp. 910–928, Mar. 2002.
20. R. Appleby and H. B. Wallace, "Standoff Detection of Weapons and Contraband in the 100 GHz to 1 THz Region," IEEE Transactions on Antennas and Propagation, **55**, pp. 2944–2956, Nov 2007.
21. Y. Yang, M. Mandehgar, and D. Grischkowsky, "Understanding THz pulse transmission in the atmosphere," IEEE Trans. THz Sci. Technol. **2**(4), 406–415 (2012).
22. H. J. Liebe, "The atmospheric water vapor continuum below 300 GHz," Int. J. Infrared Millim. Waves. **5**(2), 207–227 (1984).
23. L.S. Rothman, I.E. Gordon, A. Barbe, D. Chris Benner, P.F. Bernath, M. Birk, V. Boudon, L.R. Brown, A Campargue, J.-P. Champion, K. Chance, L.H. Coudert, V. Dana, V.M. Devi, S. Fally, J.-M. Flaud, R.R. Gamache, A. Goldman, D. Jacquemart, I. Kleiner, N. Lacome, W.J. Lafferty, J.-Y. Mandin, S. T. Massie, S.N. Milhailenko, C.E. Miller, N. Moazzen-Ahmadi, O.V. Naumenko, A.V. Nikitin, J. Orphal, V.I. Perevalov, A. Perrin, A. Predoi-Cross, C.P. Rinsland, M. Rotger, M. Simeckova, M.A.H. Smith, K. Sung, S.A. Tashkun, J. Tennyson, R.A. Toth, A.C. Vandaele, and J. Vander Auwera, "The HITRAN 2008 molecular spectroscopic database," JQSRT, **110**(9–10), 533–572 (2009).

24. H. M. Pickett, R. L. Poynter, E. A. Cohen, M. L. Delitsky, J. C. Pearson, and H. S. P. Muller, "Submillimeter, millimeter, and microwave spectral line catalog," JQSRT **60**(5), 883–890 (1998); Access to specific catalog entries may be found at http://spec.jpl.nasa.gov/.
25. Y. Yang, M. Mandehgar and D. Grischkowsky, "Broad-Band THz Pulse Transmission through the Atmosphere," IEEE Trans. THz Sci. Technol. **1**(1), 264–273 (2011).
26. Y. Yang, M. Mandehgar, and D. Grischkowsky, "Time Domain Measurement of the THz Refractivity of Water Vapor," Opt. Express **20**(24), 26208–26218 (2012).
27. H. Harde, N. Katzenellenbogen, and D. Grischkowsky, "Line-Shape Transition of Collision Broadened Lines," Phys. Rev. Lett. **74**{8), 1307–1310 (1995).
28. H. Harde, R. A. Cheville and D. Grischkowsky, "Terahertz Studies of Collision Broadened Rotational Lines, " J. Phys. Chem. A **101**(20), 3646–3660 (1997).
29. Y. Yang, M. Mandehgar and D. Grischkowsky, "Determination of the water vapor continuum absorption by THz-TDS and Molecular Response Theory," Optics Express, **22,** pp. 4388–4403 (2014).
30. R. J. Hill, "Water vapor-absorption lineshape comparison using the 22-GHz line: the Van Vleck-Weisskopf shape affirmed," Radio Science **21**(3), 447–451 (1986).
31. M. A. Koshelev, E. A. Serov, V. V. Parshin, M. Yu. Tretyakov, "Millimeter wave continuum absorption in moist nitrogen at temperature 261–328K," JQSRT **112**(17), 2704–2712 (2011).
32. M. Y. Tretyakov, A. F. Krupnov, M. A. Koshelev, D. S. Makarov, E. A. Serov, and V. V. Parshin, "Resonator spectrometer for precise broadband investigations of atmospheric absorption in discrete lines and water vapor related continuum in millimeter wave range," Rev. Sci. Inst. **80**(9), 093106 (2009).
33. T. Kuhn, A. Bauer, M. Godon, S. Buhler, and K. Kunzi, "Water vapor continuum: absorption measurements at 350GHz and model calculations," JQSRT **74**(5), 545–562 (2002).
34. V. B. Podobedov, D. F. Plusquellic, K. E. Siegrist, G. T. Fraser, Q. Ma, R. H. Tipping, "New measurements of the water vapor continuum in the region from 0.3 to 2.7 THz," JQSRT **109**(3), 458–467 (2008).
35. D. M. Slocum, E. J. Slingerland, R. H. Giles, T. M. Goyette, "Atmospheric absorption of terahertz radiation and water vapor continuum effects," JQSRT **127**, 49–63 (2013)
36. J. H. Van Vleck and V. F. Weisskopf, "On the shape of collision-broadened lines," Rev. Mod. Phys. **17**(2–3), 227–236 (1945).
37. D. Grischkowsky, Yihong Yang, and Mahboubeh Mandehgar, "Zero-Frequency Refractivity of Water Vapor, Comparison of Debye and van-Vleck Weisskopf Theory, " Optics Express**, 21**, pp. 18899–18908 (2013).
38. P. W. Rosenkranz, "Water vapor microwave continuum absorption: a comparison of measurements and models," Radio Science , **33**(4), 919–928 (1998).
39. D. Grischkowsky, S. Keiding, M. van Exter, and Ch. Fattinger, "Far-infrared time-domain spectroscopy with terahertz beams of dielectrics and semiconductors," JOSA-B, **7**(10), 2006–2015 (1990).
40. M. Mandehgar, Y. Yang and D. Grischkowsky, "Atmosphere characterization for simulation of the two optimal wireless THz digital communication links," Opt. Lett. 38 (17), 3437–3440 (2013).
41. J. H. Van Vleck, "The absorption of microwaves by oxygen," Phys. Rev. **71**(7), 413–424 (1947).
42. M. W. P. Strandberg, C. Y. Meng, and J. G. Ingersoll, "The Microwave Absorption Spectrum of Oxygen," Phys. Rev. **75,** 1524–1528 (1949).
43. G.P. Agrawal, *Fiber-Optic Communication Systems,* 3rd ed. (Wiley 2002).
44. R.W. McGowan, G. Gallot, and D. Grischkowsky, "Propagation of Ultra-Wideband, Short Pulses of THz Radiation through Sub-mm Diameter Circular Waveguides," Opt. Lett**, 24**, 1431–1433 (1999).
45. R. Mendis and D. Grischkowsky, "Undistorted guided wave propagation of subpsec THz pulses," Optics Letters**, 26,** 846–848 (2001).
46. H. T. Friis, Proc. IRE **34,** 254 (1946).
47. S. Ramo, J. R. Whinnery, and T. Van Duzer, "Fields and Waves in Communication Electronics," Third Edition (John Wiley & Sons, Inc. New York, 1993). Page 666, Eq. (7).
48. J. Lesurf, "Millimetre-wave Optics, Devices & Systems," (Adam Hilger, Bristol, UK, 1990), Eq. (4.10).
49. A.E. Siegman, "Lasers," (University Science Books, Mill Valley, CA, 1986), Chapter 17.
50. ITU-R-Model-2005, "Specific Attenuation Model for Rain for Use in Prediction Methods,"
51. R. Appleby, "Passive millimeter-wave imaging and how it differs from terahertz imaging," Phil. Trans. R. Soc. Lond. A, **362**, 379–394 (2004).
52. R.S. Lawrence and J. W. Strohbehn, "A Survey of Clear-Air Propagation Effects Relevant to Optical Communications," Proc. IEEE, **58**, 1523–1545, (1970).
53. R.W. McMillan. R.A. Bohlander, G.R. Ochs. R.J. Hill, S.F. Clifford, "Millimeter Wave Atmospheric Turbulence Measurements: Preliminary Results and Instrumentation for Future Measurements'" Optical Engineering, **22,** No. 1, 32–39 (1983).
54. R.J. Hill, R.A. Bohlander, S.F. Clifford, R.W. McMillan. J.T. Priestley, S.P. Schoenfeld, "Turbulence Induced Millimeter Wave Scintillation Compared with Micormeteorological Measurements," IEEE. Trans. Geosciences and Remote Sensing, **26,** No. 3, 330–342 (1988).

55. R.W. McMillan, "Intensity and Angle-of-Arrival Effects on Microwave Propagation Caused by Atmospheric Turbulence," IEEE International Conference on Microwaves, Communications, Antennas and Electronic Systems, 2008, COMCAS 2008.
56. M. Ruggieri, S. De Fina, M. Pratesi, A. Salome, E. Sagese, and C. Bonnifasi, "The W-Band Data Collection Experiment of the DAVID Mission," IEEE Trans. Aerosp. Electron. Syst., **38**, 1377–1387 (2002).
57. M. Lucente, E. Re, T. Rossi, E. Cianca, C Stallo, M. Ruggieri, A. Jebril, D. Dionisio, and I. Zuliani, "IKNOW mission; Payload design for in orbit test of W band technology," in Proc. IEEE Aerosp. Conf. , Big Sky. MT Mar. 1–8 (2008).
58. B. Younes, "White paper on integrated interplanetary network (IIN)," NASA Publications and Reports, Nov. 2000.
59. L. Moeller, J. Federici, K. Su, "THz Wireless Communications: 2.5 Gb/s Error-Free Transmission at 625 GHz Using a Narrow-Bandwidth 1 mW THz Source", 30th URSI General Assembly and Scientific Symposium (URSI GASS), 4 (electronic), Istanbul, (2011).
60. I. Kallfass, J. Antes, D. Lopez-Diaz, S. Wagner, A. Tessmann, A. Leuther, Broadband active integrated circuits for terahertz communication, in: Proc. of 18th European Wireless Conference European Wireless, EW, pp. 1–5 (2012)/
61. H.-J. Song, K. Ajito, Y. Muramoto, A. Wakatsuki, T. Nagatsuma, N. Kukutsu, 24 Gbit/s data transmission in 300 GHz band for future terahertz communications, IET Electron. Lett. 48 (15) 953–954 (2012).
62. S. Koenig, D. Lopez-Diaz, J. Antes, F. Boes, R. Henneberger, A. Leuther, A. Tessmann, R. Schmogrow, D. Hillerkuss, R. Palmer, T. Zwick, C. Koos, W. Freude, O. Ambacher, J. Leuthold, and I. Kallfass, "Wireless sub-THz communication system with high data rate," Nature Photonics, **7,** 977–981 (2013).